RNA 5′ terminal nucleotide determines the strength of the RIG-I/IFN signaling pathway

Magdalena Wolczyk[1*], Jacek Szymanski[1*], Ivan Trus[1*], Zara Naz[1], Agnieszka Bolembach[1], Nila Roy Choudhury[1], Tola Tame[1], Ceren Könüç[1], Elżbieta Nowak[1], Christos Spanos[2], Juri Rappsilber[3,2,4], Gracjan Michlewski[1]

* These authors contributed equally to this work.

[1] International Institute of Molecular and Cell Biology in Warsaw, Poland

[2] The Wellcome Centre for Cell Biology, University of Edinburgh, Edinburgh, UK

[3] Department of Biotechnology, Technische Universität Berlin, Berlin, Germany

[4] Si-M/"Der Simulierte Mensch", a Science Framework of Technische Universität Berlin and Charité - Universitätsmedizin Berlin, Berlin, Germany

Correspondence should be addressed to G.M. (gmichlewski@iimcb.gov.pl)

Running Title: Sequence specificity of RIG-I/IFN signaling

Key words: RIG-I, IFN type 1, 5′-triphosphate RNA guanosine (5′-pppG), 5′-triphosphate RNA adenosine (5′-pppA)

Abstract

The interferon (IFN) response is crucial for antiviral activity, but its overstimulation can lead to a wide range of autoimmune disorders. The cytoplasmic pattern recognition receptor RIG-I detects viral RNAs and endogenous polymerase III transcripts carrying a 5′-triphosphate (5′-ppp) or 5′-diphosphate (5′-pp) moiety, triggering an IFN immune response. While many viral RNAs initiate with 5′-ppp-adenosine (5′-pppA) and most endogenous Pol III transcripts in higher eukaryotes start with 5′-ppp-guanosine (5′-pppG), no apparent reason for this bias has been identified so far. Here we demonstrate that RNAs initiating with 5′-pppA trigger a much stronger RIG-I/IFN response than those starting with 5′-pppG. The structures of the matching RNA pairs have been confirmed to be similar, suggesting that functional differences in RIG-I/IFN pathway stimulation cannot be primarily explained by an altered conformation. We show that several GTP-binding proteins interact with 5′-pppG RNAs creating a steric hindrance and protecting these RNAs from activating RIG-I. Our findings suggest that 5′-pppG RNAs may allow some RNA viruses and Pol III transcripts to evade detection by cellular immune sensors. These results provide a new insight into the mechanism of sequence-dependent RIG-I/IFN pathway activation and have significant implications for understanding the antiviral response to RNA viruses and the contribution of Pol III-derived RNAs to autoimmune disorders.

Introduction

The innate immune system of higher eukaryotes is the first line of defense against invading pathogens, including viruses. Pathogen-Associated Molecular Patterns (PAMPs), which are recognized by cellular Pattern Recognition Receptors (PRRs), are shared between viral as well as endogenous RNAs. The 5′-triphosphate (5′-ppp) moiety is one such PAMP, present in many viral RNAs and endogenous polymerase III (Pol III) transcripts. [1,2] Highly structured RNAs with 5′-ppp bind to Retinoic Acid Inducible Gene I (RIG-I/DDX58) PRR, provoking its conformational change and K63 ubiquitination by E3 ubiquitin ligase RIPLET, [3,4] triggering a signaling cascade that culminates in phosphorylation of IRF3, IRF7, and NF-κB transcription factors. [5] Activated transcription factors move into the nucleus, initiating the expression of type I interferon (IFN), which in turn triggers an innate immune response. This response involves the up-regulation of numerous interferon-stimulated genes (ISGs) [6] and is crucial for antiviral activity but when overstimulated can lead to inflammation and autoimmune diseases. [7]

The most potent activators of RIG-I are short, blunt, double-stranded RNAs (dsRNAs) capped with 5′-ppp or 5′-pp. [8-11] The 5′-terminal nucleotide must remain unmethylated at its 2′-O position to be recognized by RIG-I. [12] Despite the optimal RIG-I agonist being characterized by blunt double-stranded dsRNA, experiments involving synthetic short RNA duplexes revealed that perfect complementarity is not indispensable. Short dsRNAs with short 3′ overhangs or bulge loops can also serve as potent RIG-I ligands. [9] Even synthetic dsRNAs, including RNA duplexes and short-looped RNAs, as short as 10 base pairs, proved effective in activating RIG-I. [13,14] Finally, investigations into immunogenic RNAs during Influenza A Virus infection have identified 80-nucleotide long mini viral RNAs as the most stimulatory for the RIG-I/IFN pathway. [15]

It has been noted that a substantial number of RNA viruses' genomes begin with 5′-ppp adenosine (5′-pppA) [16] and Pol III transcripts of higher eukaryotes and the genomes of some highly pathogenic RNA viruses initiate with 5′-ppp guanosine (5′-pppG). [17-21] To revisit this notion, we collated 5′-terminal nucleotides of representative RNA viruses, which are known to have 5′-ppp as well as human Pol III transcripts (Figure 1). This collection revealed that some RNA viruses (such as influenza A virus - IAV) start predominantly from 5′-pppA, whereas other pathogenic viruses (including H5N1 IAV, Ebola, Lassa, and HCV) can start from 5′-pppG or other nucleosides. Moreover, most Pol III transcripts, including non-coding tRNA, Y RNA, vault RNA, and 5S RNA, initiate from 5′-pppG. As of now, no discernible cause for this sequence bias has been determined.

Here we provide evidence that RNAs commencing with 5′-pppA elicit a considerably more robust RIG-I/IFN response in comparison to those originating with 5′-pppG. Notably, the structural configurations of these matched RNA pairs have been confirmed to be similar, implying that any variance in RIG-I/IFN pathway stimulation cannot be attributed to altered conformations. We provide evidence that several GTPases and GTP-binding proteins exhibit a specific binding affinity for 5′-pppG RNAs. This leads to a steric hindrance that shields 5′-pppG RNAs from RIG-I-mediated activation of the IFN response. Our findings suggest that 5′-pppG RNAs may enable certain RNA viruses and Pol III transcripts to evade detection by cellular immune sensors, unravelling a novel mechanism controlling sequence-dependent RIG-I/IFN pathway activation.

Results

Conserved 5′-ppp terminal nucleotide in RNA viruses and Pol III transcripts.

The terminal nucleoside at the 5′ end of mammalian Pol III transcripts is predominantly guanosine (Figure 1A). [17,18] This contrasts with transcripts of lower eukaryotes, which initiate with adenosine more frequently. [22] The genomes of human viruses with uncapped RNA genomes initiate mostly with purines (Figure 1A). While it is conventionally accepted that uncapped RNA virus genomes start with adenosine (for example IAV) (Figure 1A), [23] certain RNA viruses have adopted guanosine at the 5′ terminal position (Figure 1A and 1B). This phenomenon is observed in a diverse array of RNA viruses, including Ebola, Hepatitis C Virus (HCV), and numerous others (Figure 1B). Intriguingly, IAV reverts to its wild-type configuration upon mutation or deletion of the first nucleotide. [24] While modifying the 5′ terminal nucleotide to another purine nucleotide in hepatitis C virus (HCV) is not feasible. [20,25] Moreover, HCV genotypes starting with 5′-pppA are largely capped with flavin adenine dinucleotide (FAD), which prevents from inducing RIG-I, while genotypes starting with 5′-pppG remain uncapped. [20] The reasons for these sequences and structural preferences remain unknown.

Structures of viral and Pol III 5′-pppA and 5′-pppG RNAs

To evaluate the biological significance of the observed 5′ terminal nucleotide identity in viral and Pol III-derived RNAs, we hypothesized that retention of the 5′-pppG RNAs may be an adaptation that allows some viruses and Pol III transcripts to evade detection by the RIG-I/IFN pathway. To test this hypothesis, we employed two RNAs: IAV-derived short RNA and Pol III-derived Y5 RNA. The short viral RNA is a derivative of 3p-hpRNA (InvivoGen), a commonly used RIG-I ligand representing the first 87 nt of the positive strand of segment 8th of the IAV PR8 strain genome. By truncating 11 nucleotides from the 3′ end, we created a 76 nt RNA that

contains a blunt end panhandle structure, which is known to be an optimal RIG-I agonist and which we called short viral RNA (Figure 2A). [1,16] To see how the change of the 5′ terminal nucleotide affects Pol III transcripts, we have chosen Y5 RNA (Figure 2B). Even though the Y RNA transcripts are suboptimal RIG-I agonists with their 3′ end polyuridine tails, they have been proven to be endogenous triggers of the RIG-I/IFN pathway. [26,27] Notably, among four human Y RNAs, only Y5 RNA starts from 5′-pppA, while the three others start from 5′-pppG. It has been reported that Y5 RNA shows mainly nuclear localization, [28], and our qRT-PCR (quantitative reverse transcription and polymerase chain reaction assay)-based quantification shows that Y5 RNA levels are the lowest compared to other Y RNAs (Figure S1A). To investigate the role of the terminal nucleotide, we replaced the initial 5′-pppA with 5′-pppG in both short viral and Y5 RNAs, while maintaining the base pairing between the 5′ and 3′-ends by creating Watson-Crick base pairs (A:U and G:C) for the initial 5′-pppA or 5′-pppG (Figures 2A and 2B). All RNAs, produced by *in vitro* transcription (IVT), were purified by denaturing preparative polyacrylamide/urea gel electrophoresis (Figure S1B).

The RIG-I/IFN signaling pathway is highly dependent on RNA structure and any alterations in RNA ligand base pairing can have an inhibitory effect on the strength of the RIG-I/IFN response. [29,30] To find out if the substitution of nucleosides at the RNA ends could affect the structure of 5′-pppA *vs.* 5′-pppG RNAs, *in vitro* RNA Selective 2′-Hydroxyl Acylation analyzed by Primer Extension (SHAPE) analyses for both short viral and Y5 RNAs, were performed. Secondary structure predictions using the Maximum Free Energy (MFE) algorithm combined with SHAPE results revealed that all tested, cognate RNA pairs exhibited similar secondary structures (Figures 2A and 2B). This was supported by comparable SHAPE reactivity values for individual nucleotide positions between the 5′-pppA and 5′-pppG RNAs (Figures 2C and 2D). The Y5 RNA with 5′-pppA showed marginally more relaxed SHAPE reactivity in the bottom of the stem when compared with the 5′-pppG RNA (Figures 2C and

2D). Short viral RNA pairs were confirmed to form blunt end panhandle structures, which contain 8 bp double-stranded fragment and one mismatch between the 4th and 73rd nucleotides (Figure 2A). However, not all SHAPE reactivities fitted with the proposed structure. Mfold [31] predicts that an alternative structure, characterized by a 15 bp length, blunt end conformation, one mismatch, and a single nucleotide bulge, is expected to be the most energetically favorable (Figure S1C). Native polyacrylamide gel electrophoresis also confirmed that at least two structural conformations can be formed by short viral RNA (Figure S1D). The Y5 RNA pair were found to form long, double-stranded fragments (containing one hairpin loop, single-base bulge, and asymmetric internal loop) with a 9 nt long 3′ overhang corresponding to polyuridine tail (Figure 2B), largely similar to what has been previously described. [32]

Next, to eliminate potential confounding factors arising from RNA self-amplification via the T7 enzyme [33] and dsRNA production, [34] we conducted a comprehensive assessment of the levels of antisense strands generated by IVT (Figure S2A). Next-generation sequencing (NGS) and a two-step qRT-PCR consistently indicated an exceedingly low proportion of reads mapping to the antisense strand (<0.1% for short viral RNA and <0.4% for Y5 RNA in NGS analysis) (Figures S2A, S2B and S2C). The ratios between the sense and antisense strands for the 5′-pppA and 5′-pppG variants were found to be comparable. Strand-specific quantification of RNA through a two-step qRT-PCR approach revealed similar ΔCt values for the sense and antisense strands of the 5′-pppA and 5′-pppG variants within the cognate IVT RNAs (5′-pppA variant of short viral RNA: 14.2±0.2; 5′-pppG variant of short viral RNA: 11.5±0.1; 5′-pppA variant of Y5 RNA: M±SE = 21.0±0.9; 5′-pppG variant of Y5 RNA: 21.1±0.3 (Figure S2C)). Although trace amounts of residual contaminants from either dsDNA from the original plasmid or PCR amplicon were identified (Figures S2A and S2B), none of these contaminants elicited a type I IFN response, as assessed using the HEK-Blue assay (InvivoGen) in A549 cells (Figure S2D).

In summary, our experimental approach yielded cognate RNAs of both viral and endogenous origin, initiated with either 5′-pppA or 5′-pppG, demonstrating comparable structures and negligible levels of contaminations.

5′-pppA RNAs hyperstimulate the RIG-I/IFN pathway in human cells

To elucidate the role of the 5′ terminal nucleotide on the strength of RIG-I/IFN pathway activation, we transfected IVT short viral RNAs harboring 5′-pppA or 5′-pppG as a 5′ terminal nucleotide into human embryonic kidney HEK293 and lung adenocarcinoma A549 cells. We used a wide range of RNA concentrations between 0.1 ng/ml and 1000 ng/ml. Using IFN-α/β reporter HEK293 cells and colorimetric HEK-Blue assay, we assessed the expression of IFN-α/β that was stimulated by tested RNAs. Notably, we observed substantially more efficient activation of the RIG-I/IFN pathway by short viral RNA initiating with 5′-pppA compared to the one starting with 5′-pppG in both HEK293 and A549 cells (Figures 3A and 3B). The induction of type I Interferon was found to be dependent on the concentration of RNA. Epithelial lung A549 cells exhibited greater sensitivity to RNA compared to epithelial kidney HEK293 cells. In A549 cells, the type I Interferon response was detectable upon transfection with the 5′-pppA variants of the viral RNA starting from a concentration as low as 0.3 ng/ml, whereas in HEK293 cells, it was only registered when the RNA concentration reached 1 ng/ml. For the 5′-pppG variant of the viral RNAs type I Interferon response induction was detected starting from 30 ng/ml in both cell lines. At higher RNA concentrations (1 μg/ml), no significant difference was observed between the 5′-pppA and 5′-pppG variants. Similar findings were observed in the case of IRF3 protein phosphorylation, which was assessed with Western Blot analysis. Significant difference in the level of pIRF3 protein stimulated by 5′-pppA *vs.* 5′-pppG viral RNAs was observed for RNA concentrations ranging from 30 ng/ml to 300 ng/ml, while no difference was visible for concentrations starting from 600 ng/ml (Figure S3A).

We compared the capability of RNA to induce a type I IFN response by estimating the apparent dissociation constant (K_d) for each RNA variant. There was a 92-fold difference in apparent K_d values when comparing 5′-pppA with 5′-pppG short viral RNAs in A549 cells, and a 17-fold difference in HEK293 cells (Figures S3B and S3C). Cells exhibited significant INF production and difference between 5′-pppA with 5′-pppG short viral RNAs as early as at 4 hours into the treatment (Figures S3C-G) reaching saturation after 24 hours. Both types of RNAs (short viral RNA and Y5 RNA) initiating with 5′-pppA tested at a concentration of 100 ng/ml also proved much more potent in phosphorylating IRF3 and inducing RIG-I expression as confirmed by Western blot analysis (Figures 3C, 3D, S3E and S3G), as well as elevating type I interferon, measured with HEK-Blue assay (Figures 3A, 3B, 3E, 3F, S3D and S3F). Moreover, the original 3p-hpRNA, which does not have a blunt end, also showed similar IRF3 phosphorylation pattern in both HEK293 and A549 cells when 5′-pppA and 5′-pppG variants were compared (Figures S3H and S3I). Control experiments proved that RIG-I was essential for these RNAs to activate the pathway, as we saw no IRF3 phosphorylation in the RIG-I KO cells (Figure S4A), or when using dephosphorylated RNAs (Figures 3C-F). Similar differences in immunogenicity of 5′-pppA and 5′-pppG RNAs were observed in other human cell lines (Calu-1 and THP1; Figures S4B and S4C).

Next, to broaden our observation, we generated a collection of *in vitro* transcribed 5′-pppA and 5′-pppG RNAs predicted to differ structurally and to form blunt ends, 3′ overhang or 5′ and 3′ overhangs (the sequences and descriptions can be found in Table S1). Irrespective of the structure of RNA ends, all tested 5′-pppA RNAs (excluding full-length segment 8 of IAV strain PR8 and serine tRNA, which served here as controls) exhibited much stronger RIG-I/IFN pathway stimulation observed as a higher IRF3 protein phosphorylation in HEK293 and A549 cells (Figures S5A and S5B) and increased IFN production and activity (Figure S5C).

Together, these results show that RNAs initiating with 5′-pppA are much more immunogenic in human cells than cognate sequences starting with 5′-pppG and emphasize the significance of both RNA concentration and the duration of RIG-I/IFN pathway stimulation in this phenomenon. They also suggest a potential involvement of endogenous factors that may become saturated at very high concentrations of transfected RNAs.

5′-pppA RNAs hyperstimulate the RIG-I/IFN pathway in murine cells

To elucidate the impact of the 5′ terminal nucleotide type on the activation strength of the RIG-I/IFN pathway in murine cells, we repeated transfections with IVT RNAs in cell cultures of murine origin: murine embryonic fibroblasts cell line (MEF), primary cultures of bone marrow-derived macrophages (BMDMs) and skin-derived fibroblasts. Similarly, to human cells, western blotting analysis revealed higher levels of phosphorylated IRF3 and increased RIG-I expression for RNAs starting with 5′-pppA compared to RNAs initiating with 5′-pppG (Figures 4A and 4B). Furthermore, IVT RNAs beginning with 5′-pppA triggered the type I IFN production to a significantly greater extent than those starting with 5′-pppG in all the tested cell cultures (Figures 4C and 4D). Upon dephosphorylation of the RNAs, we were unable to detect activation of the RIG-I/IFN pathway or type I interferon responses (Figures 4A-D). Although some variation in sensitivity was observed across different cell cultures, noteworthy, the highest levels of type I IFN production were observed in BMDMs.

This observation prompted us to create a GMO mouse in which the IFN-β gene was replaced with the mKate2+ reporter (Figure S6). By replacing the IFN-β gene with the reporter we aimed to limit the IFN feedback loop, focusing mainly on the initial RIG-I/IFN pathway activation. We repeated the transfection experiments using reporter BMDM cells from homozygous mice, enabling us to monitor mKate2+ production as a representation of IFN-β expression in real time (Figure 4E). Representative images captured at 24 hours after RNA

transfection and kinetic data from mKate2+ cells illustrate that the onset of IFN-β response starts as early as at 5 hours post transfection with the response peaking at 20 hours (Figure 4F). This response was much more potent for RNAs initiating with 5′-pppA and fully triphosphate-dependent. In summary, the elevated induction of the RIG-I/IFN pathway by 5′-pppA RNAs is evolutionarily conserved.

5′-pppA RNAs hyperstimulate the RIG-I/IFN pathway *in vivo*

To test if the phenomenon of 5′-pppA RNAs hyperstimulation of the RIG-I/IFN pathway is observed in the whole animal we have injected the IVT RNAs formulated into liquid nanoparticles (RNA-LNP) into IFN-β mKate2+ reporter mice (Figure 5A). RNA-LNP complexes were injected intravenously (IV) into reporter mice within 48 h after production (Figure 5A). Twenty-four hours after administration, the red fluorescent signal (mKate2+) was observed both in the liver and spleen (Figures 5B-D). The number of cells with high mKate2+ signal was 8 and 35 times higher in mice injected with 5′-pppA compared to 5′-pppG RNA as measured by flow cytometry, in liver and spleen, respectively (Figure 5C). This shows that 5′-pppA RNA-mediated hyperstimulation of the RIG-I/IFN pathway can be also detected in the whole animal.

5′-pppG and 5′-pppA RNAs bind common and specific RBPs

To elucidate the mechanism behind the difference in the immunogenicity of 5′-pppA *vs.* 5′-pppG RNAs, we employed RNA pull-down coupled to stable isotope labelling by amino acids in cell culture (SILAC) mass spectrometry (RP-SMS), [35] identifying proteins in cell extracts that exhibited differential binding affinities to the tested RNAs. Because the technique relies on the covalent attachment of the final ribose to agarose beads, a process that could interfere with the binding of proteins like RIG-I, at first, we initially opted to employ the original 3p-hpRNA, featuring a 3′ overhang (InvivoGen). Crucially, exchanging the 5′-pppG for 5′-pppA

also rendered 3p-hpRNA significantly more immunogenic (Figures S3H and S3I). While most proteins displayed similar binding between the two RNAs, a subset of proteins emerged as outliers (Figure 6A). The 5′-pppA 3p-hpRNA pull-down enriched for RIG-I/DDX58 itself and other proteins involved in the RIG-I/IFN pathway (Figure 6B). Conversely, the 5′-pppG 3p-hpRNA pulled-down proteins associated with translation and RNA transport. A considerable proportion of proteins enriched in the 5′-pppG 3p-hpRNA pull-down possess GTP binding, small GTPase binding, or GTPase activity (Figure 6C). To further validate these findings, we employed RNA pull-down western blot analysis using HEK293 (Figure 6D) or A549 (Figure 6E) cell lysates. These results confirmed sequence-specific binding of RIG-I to 5′-pppA 3p-hpRNA and the increased binding of NUDT16, RAN, RANBP1, and EEF1A2 proteins to the 5′-pppG 3p-hpRNA. Simultaneously, no difference in binding between 5′-pppA and 5′-pppG RNAs was observed for RNA binding proteins involved in innate immune response TRIM25 [36,37] and DHX9, [38] which served as quality and quantity control proteins (Figures 6D and 6E).

Next, to test the binding of proteins to short viral RNA and Y5 RNA we employed an orthogonal approach using RNA pull-down coupled with label-free quantitative mass spectrometry (Figures 6F and 6G). These results revealed that RIG-I was present in the group of proteins that was pulled down more robustly by 5′-pppA short viral RNA or 5′-pppA Y5 RNA mirroring the data obtained with 3p-hpRNA (Figure 6A). On the other hand, the 5′-pppG short viral RNA bound a large group of proteins, among which EEF2, EEF1A1, EIF5B, NUDT16, RCC1, ERCC3, SRP68, HBS1L, LSG1, RANGAP, and TUBG1 were in common with the 5′-pppG 3p-hpRNA-pulled down proteins (Figure 6F). In the case of 5′-pppG Y5 RNA, only the RAN protein, which was found to be enriched in 5′-pppG 3p-hpRNA, was present among the bound proteins (Figure 6G). We validated these results using RNA pull-down followed by Western blotting (Figures S7A and S7B). To check the dependence of

binding of the identified proteins to the tested RNAs on the presence of the triphosphate moiety at the 5′ end of RNAs, we also tested dephosphorylated RNAs. We confirmed the sequence-specific binding of RIG-I to 5′-pppA RNAs and its strong dependence on the presence of the 5′-ppp moiety, as no RIG-I was present in the complexes with dephosphorylated RNAs (Figures S7A and S7B). Moreover, we observed that removing the 5′-ppp group from 5′-pppG RNAs resulted in complete inhibition of binding of 5′-pppG enriched proteins to dephosphorylated RNAs initiating with G (Figures S7A and S7B). This proves that the identified GTP-binding proteins and GTPases bind to RNAs using their GTP-binding pockets.

GTPase and GTP binding proteins compete with RIG-I binding to 5′-pppG RNAs

To further investigate whether the observed significant difference in RIG-I/IFN pathway activation by 5′-pppA and 5′-pppG RNAs could be a cause of impaired binding of RIG-I to the tested RNAs, fluorescence anisotropy analysis was performed to measure binding affinities of 5′-pppA *vs.* 5′-pppG short viral RNAs to purified RIG-I protein. Due to the method requirement of a fluorophore presence in the RNA molecule, internal modification with fluorescein dT (IDT) was introduced on chemically synthesized 3′ donor RNA during splint ligation with IVT 5′ acceptor RNA. Results of affinity assays indicated that RIG-I binds to the 5′-pppA short viral RNA with similar affinity of K_d = 25.7 nM to 5′-pppG RNA with the affinity of K_d = 22.6 nM (Figure 7A). This suggests that the observed mechanism of differential immunogenic potential of 5′-pppA *vs.* 5′-pppG RNAs is most likely due to sequence-specific cellular factors, which interfere with RIG-I binding to 5′-pppG RNAs leading to reduced ability to trigger the RIG-I/IFN pathway.

RNA pull-down combined with Mass Spectrometry analysis revealed that most proteins binding preferentially to 5′-pppG RNAs exhibit GTPase or GTP binding functions (Figure 6).

Thus, we hypothesized that the activity of some of the identified proteins could lead to dephosphorylation of 5′-pppG RNAs making them unable to stimulate RIG-I/IFN pathway or creating RNAs vulnerable to RNA degradation processes. To examine whether proteins enriched in the 5′-pppG RNAs pull-downs could act on them as GTPases, we investigated the phosphorylation state of RNAs after transfection. Total RNA isolated from HEK293 cells transfected with 5′-pppA or 5′-pppG short viral RNAs was treated with the 5′-3′ exoribonuclease 1 (XRN-1) enzyme, known for its specificity in degrading monophosphorylated RNAs (5′-p). To assess the effectiveness of the XRN-1 enzyme, we applied a positive control treatment, in which XRN-1 treatment was combined with the RNA 5′-Pyrophosphohydrolase (RppH) enzyme, which transforms all triphosphorylated (5′-ppp) RNAs into the monophosphorylated (5′-p) RNAs. Using qRT-PCR, we observed no significant difference in RNA abundance between both 5′-pppA and 5′-pppG variants, either in control condition or upon XRN-1 treatment. This indicates that the transfected 5′-pppA or 5′-pppG RNAs remain in the triphosphorylated state in the cells (Figure 7B). Interestingly, in co-treatment with RppH only the 5′-pppA variant was degraded, which can be explained by the sequence preference of RppH for A at the 5′ terminus of RNA. [39] *In vitro* experiments with short viral RNAs, XRN-1 and RppH substantiated our cellular-based assays (Figure 7C).

While we have demonstrated that proteins exhibiting a preference for binding to 5′-pppG RNAs do not impact their triphosphate moiety, we assumed the potential for steric hindrance in RIG-I binding. To assess the influence of GTP binding proteins on the RIG-I-RNA interaction, we introduced non-hydrolyzable GTP analogs to protein extracts during the RNA pulldown procedure. This approach aimed to occupy the GTP binding pockets, thereby impeding the GTP binding proteins interaction with 5′-pppG RNAs. Indeed, supplementation with GTP analogs led to a complete blockade of NUDT16, RAN, RANBP1, and EEF1A2 binding to RNAs. In contrast, the binding of reference proteins DHX9 and TRIM25 to RNAs remained

unaffected, as confirmed by Western blot analysis (Figure 7D). Furthermore, GTP analog supplementation resulted in comparable RIG-I binding to both 5′-pppA and 5′-pppG RNAs, unlike the strong enrichment for 5’-pppA RNA observed under normal conditions (Figures 7D and 6B). These findings substantiate that GTP binding proteins utilize a common pocket to bind both GTP and 5′-pppG RNAs.

To achieve a comparable inhibition of GTP binding proteins within cells, we enhanced GTP levels within the cells using nucleotide salvage pathway [40] by supplementation of growth medium with guanosine. [41] Thus, we performed 5′-pppA and 5′-pppG short viral RNA transfection on HEK293 cells grown for 48h on medium supplemented with guanosine or adenosine and DMSO as control conditions. We transfected 5′-pppA and 5′-pppG short viral RNAs to HEK293 cells that had been cultured for 48 hours in medium supplemented with guanosine, adenosine, or DMSO as control conditions. Upon guanosine supplementation, both 5′-pppG short viral RNA and the 5′-pppG-containing control 3p-hpRNA significantly enhanced IFN production compared to the control or adenosine treatment (Figure 7E). In contrast, the stimulation of IFN production by 5′-pppA short viral RNA was largely unaffected by the supplementation of nucleosides. These results demonstrate that the increase in GTP levels within cells can saturate GTP binding proteins, which under normal conditions bind to 5′-pppG RNA and act as a steric hindrance for RIG-I recognition.

In summary, our study demonstrates that RNAs commencing with 5′-pppA trigger a more robust RIG-I/IFN response in comparison to their corresponding counterparts initiating with 5′-pppG. This observed phenomenon is evolutionarily conserved and holds true across various tested RNAs, cell lines, and living organisms. Our working hypothesis proposes that GTPases and GTP-binding proteins impede the binding of 5′-pppG RNAs to RIG-I within the cellular environment, thereby diminishing their immunogenicity (Figure 8).

Discussion

Viruses possess a range of conserved features, including uncapped 5′-ppp termini, unmethylated CpG-rich motifs, or dsRNAs. Notably, these features are typically absent or occluded within eukaryotic hosts. These features function as targets for host innate immune system proteins, including RIG-I. [42,43] Under pathological conditions host RNAs can trigger the RIG-I pathway. [44] To prevent this, they have evolved distinct characteristics, like cap structures or nucleotide modifications, remaining largely unnoticed by the innate immune system in healthy cells. [45]

Here we propose a novel conceptual framework underlying sequence-specific RNA recognition by RIG-I and the ensuing adequate activation of the type I interferon response (Figure 8). In this model, endogenous RNAs, representing most Pol III transcripts in higher eukaryotes, and certain highly pathogenic viruses initiate with 5′-pppG. This renders them weak RIG-I agonists due to interference by GTP-binding proteins and GTPases. This and additional mechanisms, such as dephosphorylation by triphosphatase dual-specificity phosphatase 11 (DUSP11), [46] contribute to evading detection by the RIG-I signaling pathway. Conversely, RNAs commencing with 5′-pppA, characteristic of more prevalent viruses like IAV or HCV, exhibit greater potential for RIG-I/IFN activation. We have observed this phenomenon in human and mouse cultured cells as well as in the liver of whole animal injected with RNA lipid nanoparticles. Similar differences for short dsRNAs have been observed before but remain uninvestigated. [9] Substantiating these assertions is the observation that the Pol III transcript Y5 RNA, bearing 5′-pppA, is expressed at markedly lower levels compared to other Y RNAs (Figure S1A) and is retained in the nucleus. [28] Furthermore, HCV subtypes featuring 5′-pppA, but not those with 5′-pppG, employ FAD capping as a strategy to evade immune detection. [20] We speculate that the preservation of more immunogenic 5′-pppA termini in viruses might be influenced by the limitations imposed by the promoter and viral polymerase

functions. Conversely, heightened IFN signaling levels could maintain a balance in virus replication, enabling propagation without killing the host.

We noticed the induction of the type I interferon response upon transfection with 5′-pppA variants of RNAs at very low concentrations, which might represent the early stages of virus infection. In contrast, 5′-pppG variants of RNAs induced RIG-I/IFN at much higher concentrations. Additionally, at the highest RNA concentrations tested (1 μg/ml), no significant difference was observed between the 5′-pppA and 5′-pppG variants. This implies an involvement of endogenous factors that may become saturated at very high concentrations of transfected RNAs. Intriguingly, Ren *et al.* reported no difference in IFN-β induction between dsRNAs starting with 5′-pppA or 5′-pppG. [47] The observed differences with our study may be attributed to variations in the concentrations tested as well as dsRNA substrates. Ren *et al*. conducted their experiments using fully complementary, dsRNAs with two exposed ends at a concentration of 2 μg/ml. Given that their RNAs had a length of 24 nt with 10 bp, the corresponding molar concentration was approximately 259 nM. In contrast, our short viral RNA, with a length of 76 nt, exhibited optimal results at a concentration of 4.1 nM (equivalent to 100 ng/ml) and, similarly to the high concentrations tested by Ren *et al*., showed no discernible difference in IFN induction at concentrations of 41 nM and higher. Moreover, the minimal length documented thus far of the RIG-I agonist was 23 bp [16] and 10 bp. [30] We also explored IVT RNAs shorter than 76 nucleotides and observed saturation of the A to G recognition effect at 72 nucleotides (Figure S5). We postulate that, beyond base pairing considerations, the overall length of the ligand is pivotal for RIG-I recognition. Supporting a preference for longer RNAs, Velthuis *et al.* demonstrated that mini viral RNAs ranging from 56 to 125 nucleotides, derived from the IAV, exhibited the highest IFN-β promoter activity. [15] DsRNA with two exposed ends are markedly different RIG-I substrates compared to shorter single-stranded RNAs with one blunt end. We hypothesize that the former synthetic RNAs,

which are not observed in nature, could be accessed by a variety of cellular helicases, potentially altering the functional recognition by RIG-I.

A potential contamination of the IVT reaction, which can affect the immunogenicity of IVT RNAs, including mRNA vaccines, is dsRNA, resulting from promoter-independent transcription of the antisense strand. [48,49] That said, significant dsRNA production as a contaminant in the IVT requires specific optimization of the reaction. [34,50] This includes prolonged reaction time, high concentration of T7 enzyme, rNTPs mix, $MgCl_2$, and DTT, while simultaneously ensuring the absence of structures at the 3′ end. In our study, we deliberately designed dsRNA with omitted tails (for short viral RNA) or without a 3′ tail of significant length available for the polymerase (9 nt for our Y5 RNA compared to 77 nt for the pTDLS template as described in [50]). Crucially, our RNA-seq and strand-specific qRT-PCR analyses revealed comparable, minimal levels of antisense strand for both 5′-pppA and 5′-pppG RNAs (Figure S2), thereby ensuring that any disparities in RIG-I stimulation are attributed solely to the positive RNA strands.

In addition to RNA derived from RNA viruses, DNA viruses can also be a source of RNAs recognized by RIG-I. Consequently, many viruses may harbor factors that inhibit RIG-I activity. [16] Notably, RNAs from these DNA viruses (e.g., Epstein-Barr virus (EBV)) also produce RNAs with 5′-pppA termini, which could be highly immunogenic. [51] In addition, autoimmune diseases linked to EBV include systemic lupus erythematosus, [52] multiple sclerosis, [53] or rheumatoid arthritis. [54] It is suggested that EBV may contribute to the onset or exacerbation of autoimmune disorders. Despite these insights, the precise role of such RNAs in autoimmune diseases remains unclear, warranting further investigation of the complex interplay between the virus and the host's immune system.

In summary, our results indicate that RIG-I's precise identification of uncapped dsRNA in cells may depend on the existence of a distinct terminal 5′-ppp nucleotide and milieu of cellular proteins. This enhanced understanding of sequence-specific signaling within the RIG-I/IFN pathway will be crucial for gaining insights into and developing strategies to target pathogenic viruses and host RNAs that promote autoimmunity.

Materials and Methods

IVT reaction

RNA transcripts representing both viral and host origin, were prepared using IVT reaction (Supplementary Table S1). RNA representing miniviral RNA [55] was derived by truncating 76 nucleotides from segment 8th of the IAV genome (GenBank: NC_002020.1). Short non-coding Y5 RNA (84 nucleotides; GenBank: NR_001571.2) was representing the host RNA.

The transcription template was first amplified using the High-Fidelity Phusion DNA Polymerase (Thermo #F530L) and primers (Supplementary Table S2) appending T7 Class III (TAATACGACTCACTATA) or ϕ2.5 Class II (TAATACGACTCACTATT) promoter sequence to produce 5′-pppA RNA or 5′-pppG RNAs, respectively. [56] Subsequent IVT reaction producing 5′-triphosphorylated RNAs was performed with NxGen T7 RNA Polymerase (Biosearch Technologies #30223-1). For segment 8 of IAV MEGAscript T7 Transcription Kit (Thermo #AM1333) was used.

Then RNA was precipitated with 3 M Sodium Acetate (pH 5.1) and 100% EtOH, washed with 100% EtOH and resuspended in UP water. The RNA in 2× loading buffer (7 M urea, bromophenol blue, and xylene cyanol) was then run on a denaturing polyacrylamide gel (10% polyacrylamide, 7.5 M urea in 1× TBE) for 2 h. Bands were stained with Stains-all (Sigma-Aldrich #E9379) and excised with individual scalpel blades. Then RNA was extracted (0.3 M Sodium Acetate pH 5.2; 0.5 mM EDTA; 0.1% SDS) and precipitated again. Washed with

100% EtOH and resuspended in UP water. RNA concentrations were assessed with NanoDrop and adjusted to 50 ng/µl. RNA was aliquoted and stored at -80 °C. PAGE/urea gel electrophoresis was repeated to confirm that no extra bands were observed in the final RNA preparation. Dephosphorylated RNA was produced with FastAP enzyme (Thermo #EF0654) and cleaned using column purification (Invitek Invisorb Spin Virus RNA Mini Kit). The 3p-hpRNA at a concentration of 100 ng/ml (InvivoGen #tlrl-hprna) or no RNA were used as positive and negative controls, respectively.

Native polyacrylamide gel electrophoresis

For native polyacrylamide gel electrophoresis, a 10× native gel loading buffer (1 mM Tris-HCl pH 7.5, 5% glycerol, 0.001% bromophenol blue) was added to the samples and mixed. The mixtures were overlaid on a nondenaturing 12% polyacrylamide gel (prerun step was performed at 8 W for 45 min at +4 °C). After electrophoresis at 8 W for 120 min at +4 °C, the gels were stained with SYBR Gold nucleic acid gel stain (Invitrogen #S11494). Imaging was performed with a Chemidoc MP (Bio-Rad Laboratories).

Cell cultures

Murine bone marrow cells and fibroblasts were obtained from C57BL6J/Rj mice as previously described. [57,58] Bone marrow cells were cultured with 20 ng/ml of macrophage colony-stimulating factor (BioLegend #576404) for 7 days as previously described [58] to generate BMDMs. Human A549, HEK293, THP-1, Calu1, HEK-Blue IFN-α/β (InvivoGen #hkb-ifnab) cells, and murine MEF, BMDM, primary fibroblasts, B16-Blue IFN-α/β (InvivoGen #bb-ifnt1) cells were maintained in Dulbecco's Modified Eagle's Medium (DMEM; Gibco #32430) supplemented with 10% fetal bovine serum (Gibco #10270-106). HEK-Blue IFN- α/β were cultured with 100 µg/ml Zeocine (InvivoGen #ant-zn-1) and 30 µg/ml Blasticidine (InvivoGen #ant-bl-05). B16-Blue IFN-α/β cells were supplemented with 100 µg/ml of Zeocine only.

Primary cell cultures (fibroblasts and BMDMs) were established in presence of 1× Penicillin-Streptomycin (Gibco #15140122) and 0.1 mg/ml Gentamicin (Gibco #15710064). Cells were cultured at +37 °C in a 5% CO_2 humidified incubator.

Transfection of RNAs in cell cultures

Cells were seeded in a 12-well plate at a concentration of 0.3-0.7×10^6 cells per well and incubated for 24-48 hours. RNA was mixed with Lipofectamine: (100 ng RNA was prediluted in 125 µl of OptiMEM (Gibco #11058), then 2 µl of Lipofectamine 2000 (InvitroGen #11668) prediluted in 125 µl of OptiMEM was added) and after incubation at RT for 30 min 750 µl of cell culture medium was added. Leading to a final concentration of 100 ng RNA per ml of medium. RNA with medium was added to cells and incubated for 8 (A549) or 24 hours (HEK293, THP-1, Calu1, MEF, BMDM, primary fibroblasts). Supernatants and cell lysates in Roeder D Buffer (1.38 M glucose; 100 mM KCl, 2 mM EDTA; 100 mM Tris HCl pH 8; 0.2 mM PMSF and 12.5 mM DTT) were collected and processed either for IFN assay or western blotting.

IFN type 1 assay

Supernatants from murine cells (MEF, BMDM, primary fibroblasts) were processed with B16-Blue and from human (A549, HEK293, THP-1, Calu-1) with HEK-Blue cells-based assays in quadruplicates. Twenty µl of supernatants (undiluted or prediluted 1:7) were added to 50 000 of HEK-Blue or 100 000 of B16-Blue cells in a 96-well plate. A standard curve was generated in parallel by serial dilutions of recombinant IFN-β standard in DMEM (R&D Systems #8499-IF-010 and #8234-MB-010). After overnight incubation (24 h), 20 µl of supernatants were mixed with 180 µl of the working solution of the QUANTI-Blue reagent (InvivoGen #rep-qbs) and incubated at 37 °C for 0.1-3 h. Absorbance was measured at 654 nm using a Tecan's Sunrise absorbance microplate reader. Blank values were subtracted from all wells and the 4PL

standard curves were fitted to provide semiquantitative analyses of the IFN concentrations produced in the RNA-transfected cells. [59,60]

For estimating the apparent dissociation constant (K_d), first, the optical density values for the blank wells were subtracted from the experimental data. In the colour reaction controlled by alkaline phosphatase, the optical density increased at higher RNA concentrations, and the data was fitted to a four-parameter (4PL) sigmoid curve model (OpticalDensity = Bottom + (Top - Bottom) / (1 + (K_d / RNAConcentration)^Slope) with one constraint applied (Bottom = 0). To identify outliers in the dataset, Robust regression and OUTlier removal algorithm (ROUT) was employed. The false discovery rate was set at a 1% level (Q = 1%). [61] To compare K_d values between different datasets, we applied the entropy maximization principle using Akaike's Information Criterion corrected for small sample size (AICc). The probability of a shared K_d value fitting both models was computed using the relative likelihood (Akaike's Probability = 1 - 1 / (e^(ΔAICc / 2) + 1)).

Western blotting

Cell monolayers were washed once with ice-cold 1× DPBS (Gibco #14190) and resuspended in 50 µl of a Roeder D buffer (100 mM KCl, 20% (p/v) glycerol, 0.2 mM EDTA, 100 mM Tris HCl pH 8.0, 0.5 mM DTT, 0.2 mM PMSF). After vortexing, cells were sonicated with Diagenode's Bioruptor Pico sonication device for 10 min and centrifuged (10 000×g, 5 min, +4 °C). Supernatants were moved to pre-chilled low protein binding tubes and after quantifying protein concentration with NanoDrop stored at -80 °C. Twenty to hundred µg of protein extract was resolved using a 10% gel. Proteins were transferred to nitrocellulose membranes (Amersham #10600007) using a wet transfer apparatus. Membranes were blocked with 1% Western Blocking Reagent (WBR; Roche #11921681001) or 5% BSA in TBST buffer for 1 hour at room temperature. Membranes stained for pIRF3 were blocked with 5% BSA in

TBST buffer. The blocked membranes were incubated with primary antibodies diluted in 0.5% WBR in TBST overnight at +4 °C (Supplementary Table S3), washed three times with TBST, incubated with secondary antibodies diluted in 0.5% WBR in TBST for 1 hour at room temperature (Polyclonal Goat Anti-Rabbit Immunoglobulins/HRP, Agilent Dako #P0448, 1/2000), washed three times with TBST. For the chemiluminescence reaction, peroxide ECL reagents (Bio-Rad #170-5061) were applied to each band and then, the membranes were visualized using a Chemidoc MP (Bio-Rad Laboratories).

SHAPE analysis

RNA was processed with the EclipseBio SHAPE Single RNA Kit according to manufacturer's instructions. Briefly, re-folded RNA molecules were probed with NAI (2-methylnicotinic acid imidazolide), a structure probing agent, or DMSO control. Then an adapter was ligated to the 3′ end of the RNA and during reverse transcription reaction NAI induced mutations in the produced cDNA. Later, PCR-amplified libraries were subjected to Illumina 100-bp single-ended sequencing. We processed two replicates for Y5 and three replicates for short viral RNAs. For each replicate of NAI and DMSO, the data underwent the following analysis: UMI extraction with *umi_tools*, quality, and adapter trimming with *cutadapt*, repetitive element removal, alignment to hg38 using the *STAR aligner*, and PCR deduplication with *umi_tools* (10 bp UMI sequence). The specific alignment parameters were like those used by ShapeMapper2. [62] To access coverage depth reads from DMSO-treated RNA samples were split into either negative or positive strands with *samtools* and analyzed with *bedtools*.

Next, mutations (mismatches, insertions, deletions) and coverages were counted with custom Python scripts to compute mutation rates per base. Finally, NAI and DMSO mutation rates were subtracted and scaled with the interquartile range, which is the raw reactivity divided by

$1.5\times(Q_3-Q_1)$. With Q_3 and Q_1 being the 75th quartile and the 25th quartile of the raw reactivities per RNA. Reactivities for all bases with >10 000× coverage were reported.

Statistical comparison between reactivity profiles of two RNAs was conducted via the empirical Bayes (eBayes) t-test implemented in the Bioconductor package *limma*. [63] Reactivity scores per replicate were square-root transformed. Next, a standard linear model was fitted, and a t-test was performed to identify positions where both RNA molecules have significantly different reactivity scores. The eBayes method shrinks position-wise variances for the computation of t-statistics which effectively increases the degrees of freedom, and consequently, the power to identify significant differences. Finally, mean reactivity per RNA was plotted. $P < 0.001$ was considered statistically significant.

RNA extraction and qRT-PCR

RNA was extracted with Trizol (Invitrogen #15596018), and one-step qRT-PCR reactions were conducted on the Roche LightCycler 96 System. SYBRgreen-based GoTaq 1-Step qRT-PCR System (Promega #A6020) and LightCycler 96 software was used for RNA quantification. The reaction mixture (20 µl) consisted of 10 µl 2× MasterMix, 0.4 µl Reverse Transcription Mix, 0.2 µl of each primer diluted to 20 µM (Supplementary Table S4), 3.6 µl nuclease-free water and 2 µl (100 ng) of RNA template. A reverse transcription step of 15 min at 37 °C and an enzyme activation step of 10 min at 95 °C were followed by 40 amplification cycles (15 s at 95 °C and 60 s at 60 °C).

For negative strand RNA quantification with two-step qRT-PCR, RNA was first treated with DNAse I (Thermo #EN0521) following the manufacturer's instructions (60 ng of RNA per U, 30 min at 37 °C), with the addition of RNase inhibitor (Thermo #EO0381; 40 ng/U). Then after the addition of EDTA to a final concentration of 5 mM, DNAse I was inactivated by incubating at 65 °C for 10 min.

DNAse-treated RNA was subjected to SuperScript IV Reverse Transcriptase (Thermo #18090010) processing in the presence of specific forward or reverse primers, following the manufacturer's instructions (0.125 ng of RNA per U, 10 min at 53 °C). After cDNA synthesis, RNA was treated with RNase H (Thermo #EN0201; 1.25 ng of RNA per U; 20 min at 37 °C), and the RNase H activity was halted by incubating at 65 °C or 10 min.

The cDNA obtained was then processed with a SYBRgreen-based GoTaq 1-Step qRT-PCR System. The reaction mixture (10 µl) consisted of 5 µl 2× MasterMix, 0.15 µl of each primer diluted to 10 µM (Supplementary Table S4), 2.7 µl nuclease-free water and 2 µl of 1/1000 diluted cDNA template. An enzyme activation step of 200 s at 95 °C was followed by 40 amplification cycles (5 s at 95 °C and 10 s at 60 °C).

RNA pull-down and SILAC labeling

RNA pull-down assay was carried out to detect proteins binding to RNA immobilized on agarose beads. 500 pmol of *in vitro* transcribed and PAGE purified RNA was treated with 100 mM Sodium Acetate and 5 mM sodium (meta)periodate in 200 µl of water and rotated for 1 h at room temperature in the dark. The RNA was precipitated by adding 600 µl of 100% ethanol and 15 µl of 3 M Sodium Acetate and incubating on dry ice for 30 min, followed by centrifugation at 16 000×g, +4 °C for 20 min. The RNA pellet was washed with 70% ethanol, followed by 5 min centrifugation at 16000×g and resuspended in 500 µl of 100 mM Sodium Acetate pH 5.2.

For one reaction 250 µl of adipic acid dihydrazide-agarose beads (Sigma-Aldrich #A0802) were washed 3× with 100 mM Sodium Acetate followed by centrifugation at 2000×g, +4 °C for 2 min, then mixed with 500 µl of the periodate oxidized RNA and incubated overnight at +4 °C in the dark with rotation. The RNA-beads were washed by mixing with 700 µl of 4 M KCl and rocking for 30 min at room temperature and centrifuged at 2000×g for 5 min, then

washed 2× with 2 M KCl, 2× with Buffer G (20 mM Tris-HCl pH 7.5, 137 mM NaCl, 1 mM EDTA, 1% Triton X-100, 10% glycerol, 1.5 mM $MgCl_2$, 1 mM DTT and 200 μM PMSF) and 1× with Roeder D followed by 2 min centrifugation at 2000×g. Control beads with no RNA attached were also prepared.

One mg of total protein extract was added to RNA-beads. The mixture was supplemented with 1.5 M $MgCl_2$, 25 mM creatine phosphate, 100 mM ATP, and 2.5 μl of RiboProtect Hu RNase Inhibitor (Blirt #RT35). Additionally, for GTP analog treated samples Non-hydrolyzable GTP Test Kit (Jena Bioscience #NK-102) containing 5 analogs – GTPαS, GpCpp, GppCp, GppNHp, GTPγS – was used. Each GTP analog was supplemented in 0.1 mM final concentration, which multiplied by 5 results in 0.5 mM GTP analogs in total and corresponds to average GTP concentration in mammalian cells. [64] The mixture volume was adjusted to 650 μl with nuclease-free water. The RNA-beads-cell lysates mixtures were incubated at 37 °C for 30 min with shaking. After 3 washes with Buffer G, the beads were mixed with 60 μl of 5× Sample Buffer. Proteins captured by RNA were denatured at 95 °C for 10 min with shaking. Thirty μl of the supernatant was loaded onto SDS-PAGE or NuPAGE gel and western blot or mass spectrometry analysis was performed to detect the proteins respectively.

The RNA pulldown coupled with SILAC mass spectrometry was executed following established protocol. [35] In brief, HeLa cells were cultured in SILAC media (DC Biosciences), designated as 'heavy' or 'light', and supplemented with dialyzed calf serum (DC Biosciences) to incorporate heavy or light isotopes into the cells. Cell extracts were prepared and incubated with RNA (Dharmacon) attached to agarose beads. Specifically, 5′-pppA RNA was incubated with 'heavy' extract, while 5′-pppG RNA was incubated with 'light' extract. In a parallel experiment, 5′-pppA RNA was incubated with 'light' extract, while 5′-pppG RNA was incubated with 'heavy' extract.

Mass spectrometry

Proteins were separated on gel (NuPAGE Novex 4-12% Bis-Tris gel, Life Technologies), in NuPAGE buffer (MES) for 10 min and visualised using InstantBlue stain (Abcam). The stained gel band was excised and de-stained with 50 mM ammonium bicarbonate (Sigma Aldrich) and 100% (v/v) acetonitrile (Sigma Aldrich) and proteins were digested with trypsin, as previously described. [65] In brief, proteins were reduced in 10 mM dithiothreitol (Sigma Aldrich) for 30 min at 37 °C and alkylated in 55 mM iodoacetamide (Sigma Aldrich) for 20 min at ambient temperature in the dark. They were then digested overnight at 37 °C with 13 ng/µl trypsin (Pierce). Following digestion, samples were diluted with an equal volume of 0.1% TFA and spun onto StageTips as described by Rappsilber *et al.* [66] Peptides were eluted in 40 µl of 80% acetonitrile in 0.1% TFA and concentrated down to 1 µl by vacuum centrifugation (Concentrator 5301, Eppendorf). They were then prepared for LC-MS/MS analysis by diluting it to 5 µl by 0.1% TFA.

LC-MS analyses were performed on an Orbitrap Exploris 480 (SILAC experiments) and an Orbitrap Fusion Lumos (label-free quantification) mass spectrometers (Thermo) coupled with an Ultimate 3000 HPLC (Dionex, Thermo). Peptides were separated on a 50 cm (2 µm particle size) EASY-Spray column (Thermo), which was assembled on an EASY-Spray source (Thermo) and operated constantly at 50 °C. Mobile phase A consisted of 0.1% formic acid in LC-MS grade water and mobile phase B consisted of 80% acetonitrile and 0.1% formic acid. Peptides were loaded onto the column at a flow rate of 0.3 µl/min and eluted at a flow rate of 0.25 µl/min according to the following gradient: 2 to 40% mobile phase B in 150 min and then to 95% in 11 min. Mobile phase B was retained at 95% for 5 min and returned to 2% a one minute after the end of the run (160 min). For the label-free experiment, LC conditions were similar, but the gradient was extended at 150 min with total run time at 190 min per injection.

For our SILAC experiment, MS1 scans on Orbitrap Fusion™ Lumos™ were recorded at 120,000 resolution (scan range 350-1500 m/z) with an ion target of 4.0e5, and injection time of 50ms. MS2 was performed in the ion trap at a rapid scan mode, with ion target of 2.0E4 and HCD fragmentation [67] with normalized collision energy of 27. The isolation window in the quadrupole was 1.4 Thomson. Only ions with charge between 2 and 6 were selected for MS2. Dynamic exclusion was set at 60 s.

For Exploris™ 480, survey scans were recorded at 120,000 resolution (scan range 350-1650 m/z) with an ion target of 5.0e6, and injection time of 20ms. MS2 Data Independent Acquisition (DIA) was performed in the orbitrap at 30,000 resolution with a scan range of 200-2000 m/z, maximum injection time of 55ms and AGC target of 3.0E6 ions. We used HCD fragmentation [67] with stepped collision energy of 25.5, 27 and 30. The inclusion mass list with the correspondent isolation windows is shown in the table below. Data for both survey and MS/MS scans were acquired in profile mode.

The MaxQuant software platform [68] version 1.6.1.0 was used to process the raw files from the SILAC labelled samples and the search was conducted against the complete/reference proteome set of *Homo sapiens* (Uniprot database - released in 2019), using the Andromeda search engine. [69] For the first search, peptide tolerance was set to 20 ppm while for the main search peptide tolerance was set to 4.5 pm. Isotope mass tolerance was 2 ppm and maximum charge to 7. Digestion mode was set to specific with trypsin allowing maximum of two missed cleavages. Carbamidomethylation of cysteine was set as fixed modification. Oxidation of methionine was set as variable modification. To account for the SILAC labels, multiplicity was set to 2, with lysine +4 and arginine +6 selected.

The DIA-NN software platform [70] version 1.8.1. was used to process the raw files from label-free DIA and the search was conducted against the *Homo sapiens* database (Uniprot, released

in 2019). Precursor ion generation was based on the chosen protein database (automatically generated spectral library) with deep-learning based spectra, retention time and IMs prediction. Digestion mode was set to specific with trypsin allowing maximum of one missed cleavage. Carbamidomethylation of cysteine was set as fixed modification. Oxidation of methionine, and acetylation of the N-terminus were set as variable modifications. The parameters for peptide length range, precursor charge range, precursor m/z range and fragment ion m/z range as well as other software parameters were used with their default values. The precursor FDR was set to 1%.

Statistical analysis was performed with R [R Core Team (2021). R: A language and environment for statistical computing. R Foundation for Statistical Computing, Vienna, Austria. URL https://www.R-project.org/.]. *Protti* R package [71] was used for quality control, data filtration, imputation of missing values, and statistical significance calculation using a moderated t-test based on the *limma* R/Bioconductor package [63]. For functional validation, P-values were adjusted for multiple testing with the Benjamini-Hochberg correction. Data visualisation was performed using the *ggplot2* R package.

Generating mice line harboring a fluorescent marker mKate2 in the IFN-β gene

A genetically modified mouse line was created in the Genome Engineering Unit at the International Institute of Molecular and Cell Biology (https://crisprmice.eu/).

The mKate2 fluorescent marker nucleotides sequence, optimized for the mouse genome was inserted at the beginning of the IFN-β coding sequence [GenBank: NM_010510.2] using the CRISPR/*Cas9*-based methodology as previously described. [72] Briefly, C57BL6J/Rj zygotes were microinjected with *Cas9* mRNA (25 ng/µl), sgRNA (GGUAGCAGCCGACACCAGCC; 12.5 ng/µl), and repair template dsDNA with 60 bp homology arms. To ensure proper transcription termination, two SV40 early mRNA

polyadenylation signal sequences were added after the mKate2 sequence. An additional G>C mutation in the 5′ UTR was introduced to destroy the PAM sequence. Zygotes were surgically transferred to surrogate females and pups were screened by the PCR method using primers flanking the inserted sequence (forward primer: TGGGAAATTCCTCTGAGGCAG; reverse primer: AGGCAGTGTAACTCTTCTGCATC) and the presence of the correct insert (Suppl. Fig. S6) was confirmed through Sanger sequencing. Founder mice were backcrossed with wild-type mice to get N1 generation animals. For routine genotyping, DNA from ear tips was extracted using the HotShot method, [73] and a 3-primer method was used for PCR (forward primer: TGGGAAATTCCTCTGAGGCAG; reverse primer #1: AGGCAGTGTAACTCTTCTGCATC; reverse primer #2: TTACCGGTGGCCGAGCTTAC).

Mice were bred and maintained in the animal facilities of the IIMCB under standard conditions with the approval of the Polish Ministry of the Environment (decision #29/2023). The housing conditions in ventilated cages (Tecniplast #EM500) filled with wood chip bedding, enriched with nesting material, plastic houses, and cardboard tubes were in adherence with the Regulation of the Minister of Agriculture and Rural Development of 29 April 2022.

Mice were provided *ad libitum* with water and rodent feed (Altromin #1324TPF). The environmental conditions included a relative humidity of 45-65% and a room temperature of 20-24 °C. The ventilation system ensured 75 air changes per hour for each cage. The lighting schedule followed a 12-hour light/12-hour dark cycle (lights on from 6:00 to 18:00).

Regular health monitoring was conducted at the IDEXX laboratory, and all animal procedures adhered to the guidelines of the EU Directive #2010/63/EU for animal experiments.

RNA encapsulation into lipid nanoparticles.

Lipid mix composition (50:10:38.5:1.5 molar ratio of DLin-MC3-DMA:DSPC:Cholesterol:PEG2000-DMG) was composed as previously described. [74] RNA

was encapsulated with a vortex mixing method (3:1 vol:vol ratio of RNA to lipid) and the N/P ratio (cationic nitrogen groups from the ionizable lipid over anionic phosphate groups from the mRNA) was ~3. Buffer was exchanged for 1× DPBS and LNPs were concentrated by centrifugation on Amicon 50 kDa filter unit (Merck #UFC805024). Size distribution and polydispersity index were determined using dynamic light scattering on Zetasizer Ultra Red (Malvern) in PBS buffer at 25°C in backscatter mode. Encapsulation efficiency and concentration of mRNA entrapped in LNPs were determined using the Quant-iT Ribogreen RNA assay (Invitrogen #R11490) by comparing fluorescence intensities in the presence or absence of 0.1% (w/v) Triton X-100.

IV injection of RNA-LNP complexes in reporter mice and preparing cell suspensions

The study protocol (#WAW2/124/2023) was approved by the 2nd Local Ethics Committee for Animal Experimentation in Warsaw. Randomly selected IFN-β/mKate2+ heterozygous male animals over 6 weeks of age were intravenously injected with 100 µg/kg of RNA encapsulated into LNP-RNA complexes and resuspended in sterile 0.85% NaCl up to 60 µl. In 24 hours, animals were euthanized with CO_2 and exsanguinated. The spleen and liver were extracted, minced with scissors, and pressed through a 70 µm strainer (Corning #431751) in the presence of ice-cold HBSS (Gibco #14025092). Cells were centrifuged at 200×g for 3 min at 4 °C and the pellet was washed. Red blood cell depletion was made with lysis buffer (BioLegend #420301) according to manufacturer's recommendations.

Flow cytometry

Flow cytometry was performed on a Beckman Coulter CytoFLEX flow cytometer. Data acquisition and analysis were done with Beckman Coulter CytExpert 2.3 software. Dead cells were excluded from the analysis using live/dead Fixable Violet Dead Cell Stain Kit (Life Technologies #L34955) according to the manufacturer's protocol. Life/dead stain was excited

using a 405 nm laser and the signal was detected using a 450/45 detector. mKate2 was excited using a 561 nm laser and the signal was detected using a 610/20 detector. The compensation matrix for relevant channels was calculated by the software. For the 450/45 detector the compensated value was 14.57 and for the 610/20 detector the compensated value was 1.4. One million events were collected per sample.

Image acquisition and analysis with Opera Phenix

BMDM plated in 96-well plates (Greiner Bio-One #655090) at a density of 10^4 cells per well were subjected to lipofection with RNAs. Then nine non-overlapping images per well with a resolution of 1080×1080 were captured on an hourly base using a 10× objective and 2× binning in non-confocal mode on the PerkinElmer Opera Phenix High-Content Screening System. Image acquisition and quantitative analysis were performed using the built-in software, Harmony 4.9. The chamber temperature was maintained at 37 °C, with CO_2 levels set at 5%.

Before analysis, flat-field correction was applied and, subsequently, cells were segmented based on the mKate2 signal. The subpopulation of cells with 150-800 μm^2 of area occupied that started to exhibit mKate2 signal with a mean intensity of ≥400 was counted.

RIG-I CRISPR/*Cas9* knockout

HEK293 cells were co-transfected with 200 ng of GeneArt CRISPR Nuclease mRNA (Invitrogen #A29378) in addition to sgRNA prepared by mixing fluorescently labelled Alt-R CRISPR-*Cas9* tracrRNA, ATTO 488, (IDT #10010170) with Alt-R CRISPR-*Cas9* crRNA targeting sequence in intron 1 of DDX58 gene encoding RIG-I protein (IDT #Hs.Cas9.DDX58.1.AA – GGAUUAUAUCCGGAAGACCC) at a 4 nM final concentration. After 24 hours, fluorescence-positive cells were sorted using BD FACSAria II cell sorter to a 96-well plate at a seeding concentration of one cell per well, and the cells were

grown in penicillin/streptomycin (Gibco #15140-122) containing DMEM until single colonies were established. Next, cells were split into two 96-well plates, one of which was used for a dot blot analysis. For the dot blot analysis, cells were washed once in cold PBS before adding 20 µl of Roeder D Buffer per well and sonication for 10 min (30 sec ON/30 sec OFF). Six microliters of protein from each well were spotted directly onto a nitrocellulose membrane followed by western blotting. Selected clones were seeded from the second 96-well plate into 6-well plates and grown. The RIG-I levels were validated by standard western blotting. Recombinant human IFN-β (R&D Systems #8499-IF-010) treatment was used to induce RIG-I expression and to correctly select clones with the lowest RIG-I level. This strategy led to the creation of three HEK293 cell clones with RIG-I knock-out.

Production of the recombinant RIG-I protein

Gene coding RIG-I/DDX58 cDNA [GeneID: 23586] was cloned in pET28-6xHis-SUMO vector (Thermo #K30001). Protein was expressed in *E. coli* BL21-RIL cells (Agilent #230245) cultivated in Lysogeny Broth medium overnight at 18°C after induction with 0.4 mM isopropyl β-D-1-thiogalactopyranoside at OD 06-07. The harvested cells were pelleted by centrifugation at 4000×g, 4 °C for 20 minutes and resuspended in buffer A (50 mM HEPES buffer pH 7.5, 500 mM NaCl, 10% glycerol, 5 mM β-mercaptoethanol, 20 mM imidazole and 40 mM L-arginine) supplemented with proteinase inhibitors, and sonicated. The lysate was then subjected to ultracentrifugation at 100’000×g, 4 °C for 40 min yielding a clear supernatant. The clarified lysate was applied on a 5 ml His-Trap HP column (Cytiva #17524802) pre-equilibrated with buffer A. The column was washed with buffer A, followed by a wash with the same buffer that included 60 mM imidazole, RIG-I protein was eluted with buffer A that contained 500 mM imidazole. To remove the 6xHis-SUMO tag, the fusion protein was digested with SUMO protease and dialyzed overnight against buffer A at 4 °C. The cleaved SUMO protein was removed on a His-Trap HP column. For the final purification step, tag-free

RIG-I from the flow-through was applied to a size exclusion column Hiload 16/600 Superdex 200 (Cytiva #28989335), pre-equilibrated with buffer A without imidazole. The RIG-I protein fractions were pooled and concentrated using a 30 kDa Amicon Ultra filter (Millipore #UFC903008). Lastly, the concentration of RIG-I was measured with NanoDrop and the purified protein was stored at -80 °C.

Splint ligation

Internally fluorescein-labelled RNA was produced by ligation of *in vitro* transcribed 5′ acceptor RNA fragment with chemically produced 3′ donor RNA containing internal fluorescein dT modification and 5′ monophosphate essential for ligase activity using T4 Ligase 2 (NEB #M0239S). Additionally, the ssDNA fragment complementary to the 3′ end of the acceptor and the 5′ end of the donor was used as a splint to increase the specificity of ligation. Ligation was performed according to the manufacturer protocol for the T4 Ligase 2 enzyme. Ligated RNA was precipitated and purified from PAGE/urea gel with the procedure described in the **IVT reaction** section.

Fluorescent anisotropy

RNA-protein binding assays were performed in a binding buffer (50 mM Tris-HCl pH 7.5, 150 mM NaCl, 10% glycerol, 1.5 mM $MgCl_2$, 0.5 mM ATP, 20 mM arginine, 1.5 mM DTT). First, 5 nM fluorescein-labelled RNA solutions were prepared in binding buffer and RNA was refolded by incubating for 10 min at 85 °C and cooling down in room temperature for at least 15 min. Then 5 µl of 5 mM RNA solution and 40 µl of binding buffer were transferred into a 96-well plate. Five µl of protein samples in different concentrations were added to RNA and mixed by gentle pipetting. Anisotropy was determined with a TECAN Infinite M1000 plate fluorimeter. For FITC, wavelengths were set to 495 nm for excitation and 520 nm for emission. Anisotropy values for RNA samples without protein were subtracted. To obtain binding affinity

results for each RNA variant, outcomes were fitted to the 4PL regression model. The dissociation constant (K_d) was calculated as the concentration of protein, at which anisotropy reaches half of the equilibrium state value.

5′-end phosphorylation state analysis

HEK293 cells were transfected with short viral RNA and incubated for 24 hours. After incubation total RNA was extracted with Trizol, DNA was removed using DNase I treatment and RNA was purified with GeneJET RNA Cleanup and Concentration Micro Kit (Thermo #K0841). Then, 1 mg of purified total RNA sample was treated in three different conditions – without enzyme, with XRN-1 (NEB #M0338S) alone, or with XRN-1 and RppH (NEB #M0356S) together. Reactions were performed at 37 °C for 60 min in dedicated buffer for XRN-1 enzyme provided by the producer. Then, treated samples were processed with RNA clean-up again and prepared for quantification analysis by cDNA synthesis using microScript microRNA cDNA Synthesis Kit (Norgen Biotek #54410). Quantities of short viral RNA upon treatment were measured with one-step qRT-PCR assay with β-actin mRNA as a reference RNA.

Induction of nucleotide salvage pathway

To elevate the GTP level in the cells, HEK293 48-well cell cultures were supplemented with 100 μM guanosine (Sigma Aldrich #G6264). DMSO and 100 μM adenosine (Sigma Aldrich #A9251) treatments were utilized as control conditions. The cells were incubated for 48 h in cell culture incubator, and then transfected with RNAs. After 24 h incubation, supernatants were collected for IFN assay, and the cells were lysed in lysis buffer and used for Western blot analysis.

Statistical analysis

All data are reported as mean ± standard deviation. Statistical analyses were performed using GraphPad Prism 10.1.1.

Data Availability

The data presented in the study are deposited in the Sequence Read Archive repository, BioProject accession number PRJNA1054022. The mass spectrometry proteomics data have been deposited in the ProteomeXchange Consortium via the PRIDE [75] partner repository with the dataset identifier PXD048038. Supplementary data available on-line.

Acknowledgments

We thank dr Olga Gewartowska and mgr. Marcin Szpila for their invaluable assistance with GMO mice. Additionally, we extend our thanks to dr Łukasz Majewski and dr Piotr Jan Korzeniowski and Damian Komorowski for their excellent support with animal trials. We thank prof. dr hab. Jacek Jemielity and dr Marek Baranowski from ExploRNA for invaluable assistance with encapsulating RNA into lipid nanoparticles. We thank dr Katarzyna Mleczko-Sanecka and Raghunandan Mahadeva for help in establishing cell cultures of BMDMs. Figures 5 and 8 were created with BioRender.com.

Author contributions

G.M. conceived this study; G.M., J.R., E.N., M.W., J.S., and I.T. designed the experiments; M.W., J.S., I.T., A.B., N.R.C., Z.N., T.T., C.S. and C.K. performed experiments; G.M, J.R., C.S. E.N., I.T., J.S., and M.W. analyzed data; G.M., M.W., J.S., and I.T. wrote the manuscript with input from other authors. All authors read and approved the final manuscript.

Funding

Project financed under DIOSCURI, a programme initiated by the Max Planck Society, jointly managed with the National Science Centre in Poland, and mutually funded by Polish Ministry of Science and Higher Education and German Federal Ministry of Education and Research [2019/02/H/NZ1/00002 to G.M.]; Polish National Agency for Academic Exchange within Polish Returns Programme as well as National Science Centre [2021/01/1/NZ1/00001 to G.M.]. This work was financed by the statutory funding of the International Institute of Molecular and Cell Biology in Warsaw. J.R. was funded by the Deutsche Forschungsgemeinschaft (DFG, German Research Foundation) under Germany′s Excellence Strategy – EXC 2008 – 390540038 – UniSysCat and project 449713269. The Wellcome Centre for Cell Biology is supported by core funding from the Wellcome Trust (Grant number 203149). C.S. was funded by Wellcome instrument grant 108504. Funding for open access charge: DIOSCURI Centre.

Competing interests

The authors declare no competing interests.

Figures

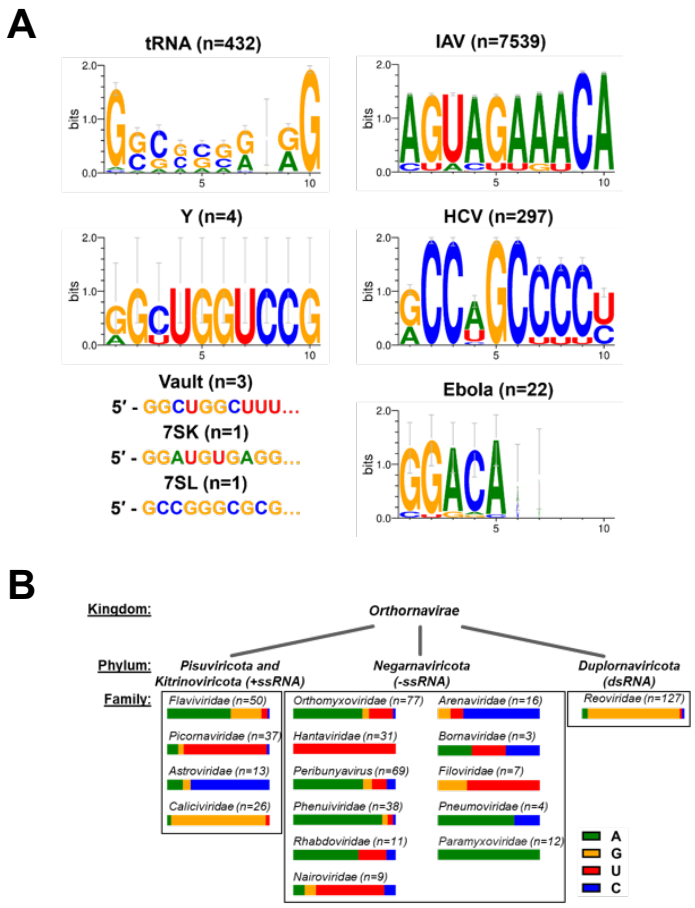

Fig. 1. Terminal 5′-ppp nucleotide conservation in viruses and Pol III transcripts. (**A**) The conservation of the terminal 5′-ppp nucleotide in both Pol III transcripts and selected human viruses with uncapped RNA genomes. Nucleotide sequences representing the 5′ end of specific Pol III transcripts and selected RNA viruses. The sequence probability logos were generated using WebLogo 3. [76] The data sources include GenBank, tRNAscan-SE Genomic tRNA Database (http://gtrnadb.ucsc.edu/), and for Ebola. [21] (**B**) Variability in the 5′ nucleotide of human viruses with uncapped RNA genomes. 5′ terminal nucleotides of uncapped RNA viruses. The reference sequences of viral genomes were downloaded from the NCBI Viral Genome Browser (https://www.ncbi.nlm.nih.gov/genome/viruses/). The numbers in parentheses indicate the number of genomes/segments represented per family. The frequencies of initial nucleotides are depicted using horizontal bars.

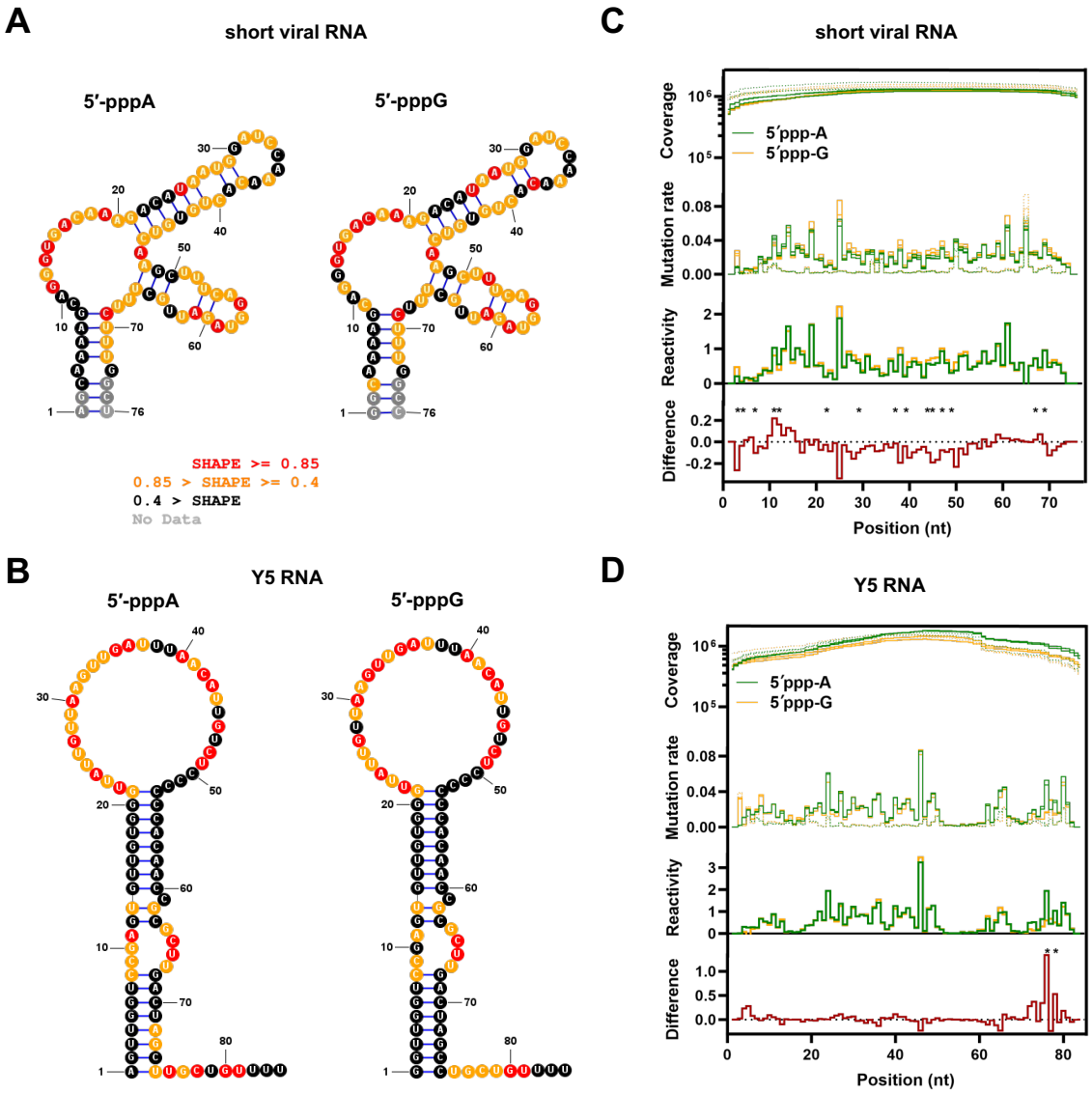

Fig. 2. Results of SHAPE analysis conducted for short viral RNA representing fragment of segment 8 of IAV genome and host Y5 RNA. (**A**, **B**) IVT RNAs starting either from 5′-pppA or 5′-pppG were subjected to SHAPE analysis. Secondary structures representing viral RNA and Y5 were predicted using the MFE algorithm with SHAPE constraints specified. [77] (**C**, **D**) Sequencing coverage exceeded the minimal threshold (10 000×) in all replicates of NAI-treated samples (solid lines) and DMSO-treated samples (dotted lines). The mutation rate was higher in NAI-treated samples (solid lines). Corresponding spikes in mutation, found in NAI and DMSO samples, might indicate a single-nucleotide polymorphism in the sample compared to the reference genome. All individual replicates (**C**: n = 3 for short viral RNA; **D**:

n = 2 for Y5 RNA) are shown both in coverage and mutation line plots. The following part of the plot shows overlayed average reactivity levels between the set of RNAs. Higher SHAPE reactivity scores across the RNA of interest correlate with a higher likelihood of being unpaired. Negative reactivity values are excluded from the plot. The following part of the plot shows the difference between positive reactivity scores. Positions where reactivities are significantly different ($P < 0.001$) for A variant *vs.* G variant comparison are marked with an asterisk (*).

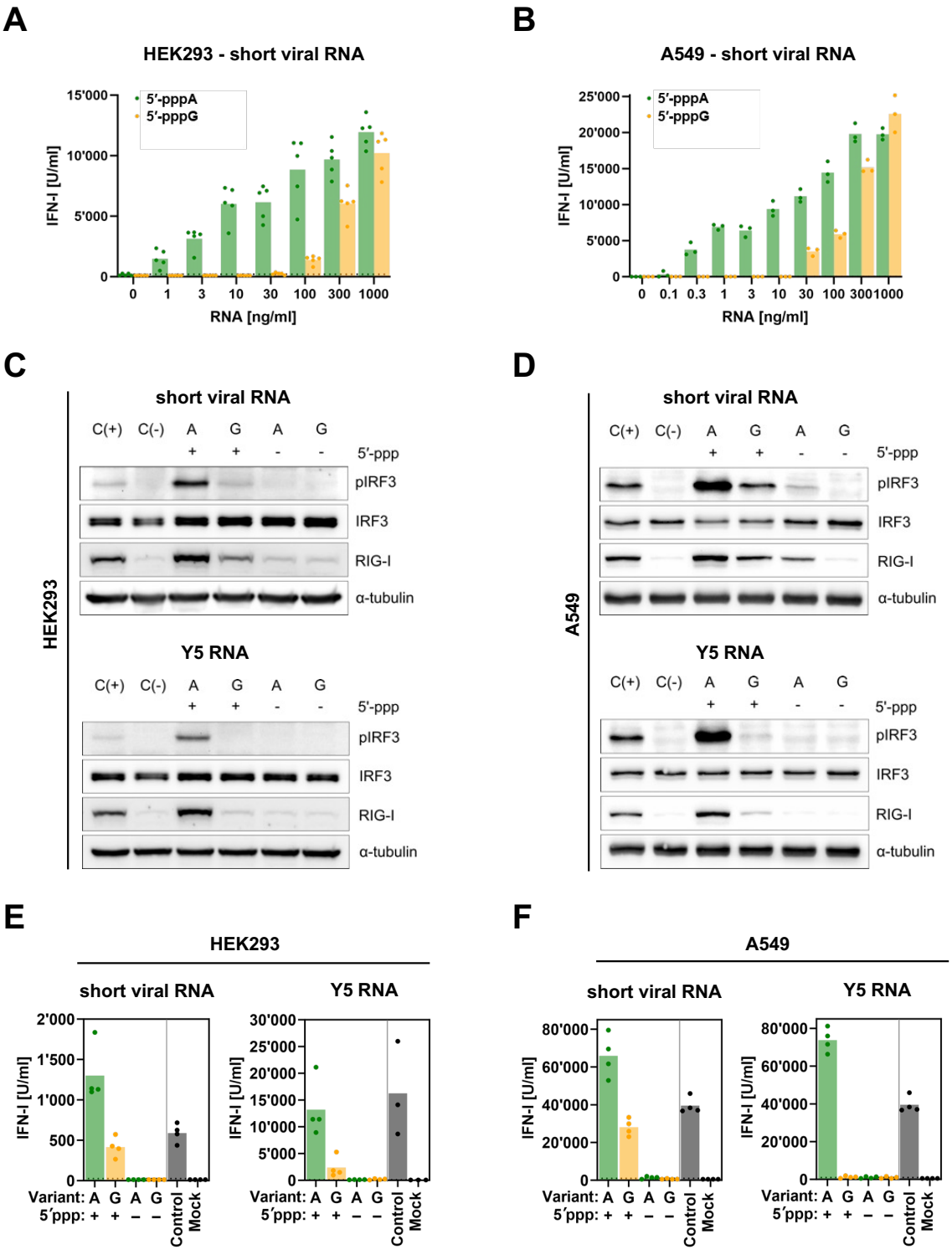

Figure 3. Comparison of RIG-I/IFN responses against RNAs starting from 5′-pppA and 5′-pppG in human cell lines. (**A**) To compare the RIG-I/IFN responses triggered by RNAs that begin with 5′-pppA and 5′-pppG, IVT RNA, representing a fragment of the IAV genome, was transfected into HEK293 cells at various concentrations. The concentrations of type I IFN

in the supernatants were assessed using the HEK-Blue assay after 24 hours. A selected concentration of RNA (100 ng/ml) was used to assess RIG-I levels and IRF3 phosphorylation with western blotting upon treatment. (**C**) Dephosphorylated viral RNA (100 ng/ml) and Pol III transcript Y5 RNA were subjected to the HEK-Blue assay. (**B, D, F**) Similar experiments were conducted in A549 cells, with type I IFN concentrations assessed in the supernatants and RIG-I levels and IRF3 phosphorylation in protein lysates in 8 hours after treatment. The dotted line represents a lower quantification limit.

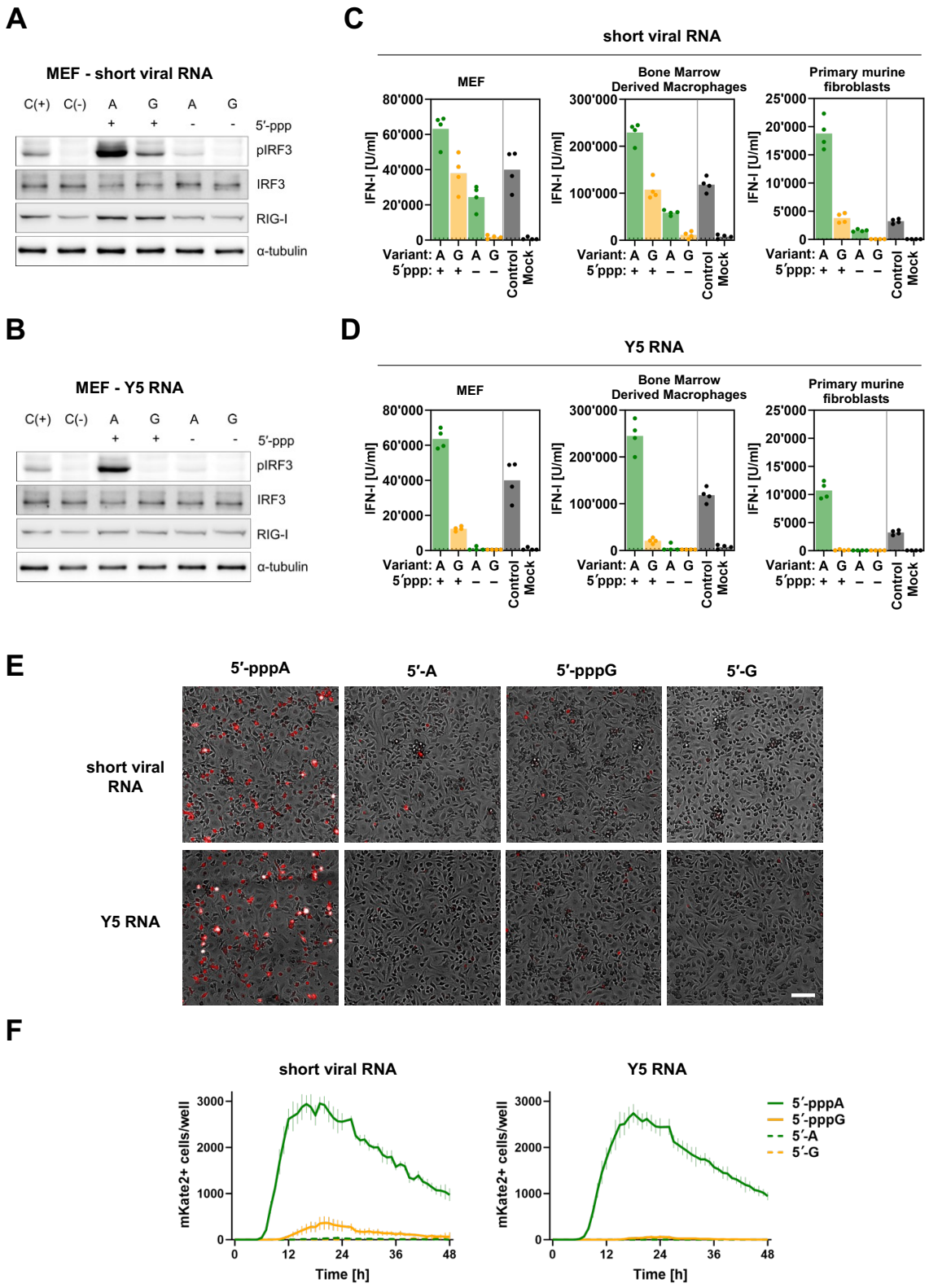

Fig. 4. Comparison of RIG-I/IFN responses against RNAs starting from 5′-pppA and 5′-pppG in cell cultures of murine origin. To compare the RIG-I/IFN responses triggered by RNAs that begin with 5′-pppA and 5′-pppG, IVT RNA, representing a fragment of the IAV

genome, and Pol III transcript Y5 RNA were transfected into murine cells at a concentration of 100 ng/ml. (**A, B**) RIG-I levels and IRF3 phosphorylation in protein lysates were assessed using western blotting. (**C, D**) The concentration of type I IFN in the supernatants was measured using IFN assay at 24 hours after treatment. The dotted line represents a lower quantification limit. (**E**) Representative images of murine mKate+ BMDMs at 24 hours upon RNA transfection. (**F**) Counts of mKate2+ cells at 0-48 hours upon RNA transfection. Scale bar is 100 μM. Vertical lines represent standard deviation for n = 4.

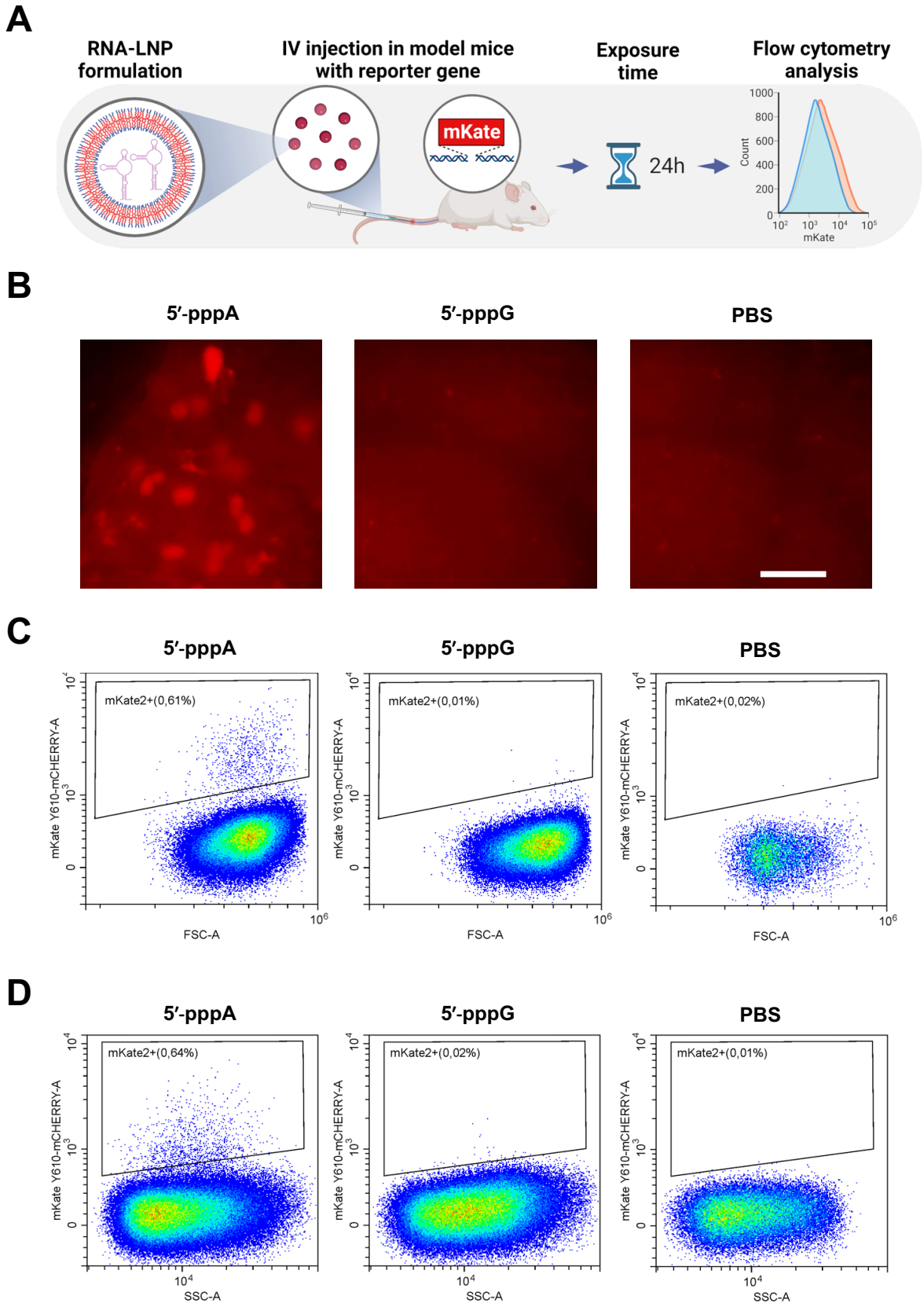

Fig. 5. Comparison of RIG-I/IFN responses against RNAs starting from 5′-pppA and 5′-pppG *in vivo*. (**A**) Experimental setup: RNA was encapsulated into LNP and RNA-LNP

complexes were IV injected (100 µg of encapsulated RNA per kg of body weight) in mice. Flow cytometry analysis of hepatocytes from reporter mice was conducted 24 hours after RNA-LNP inoculation. (**B**) Fluorescent cells in liver. The injection of the 5′-pppA variant of short viral RNA allowed the observation of fluorescent cells in liver before processing the organs into cell suspension. Scale bar is 50 µm. (**C, D**) Representative images for flow cytometry analysis of hepatocytes and splenocytes. (**C**) Liver: P = 0.0005 using one-way ANOVA with Šídák's multiple comparisons test; 5′-pppA: M±SD = 0.81±0.17%, n = 3; 5′-pppG: 0.11±0.06%, n = 2; PBS control: 0.19±0.12%; n = 5. (**D**) Spleen: P = 0.028 using one-way ANOVA with Šídák's multiple comparisons test; 5′-pppA: M±SD = 0.40±0.29%, n = 3; 5′-pppG: 0.01±0.01%, n = 2; PBS control: 0.01±0.01%; n = 5.

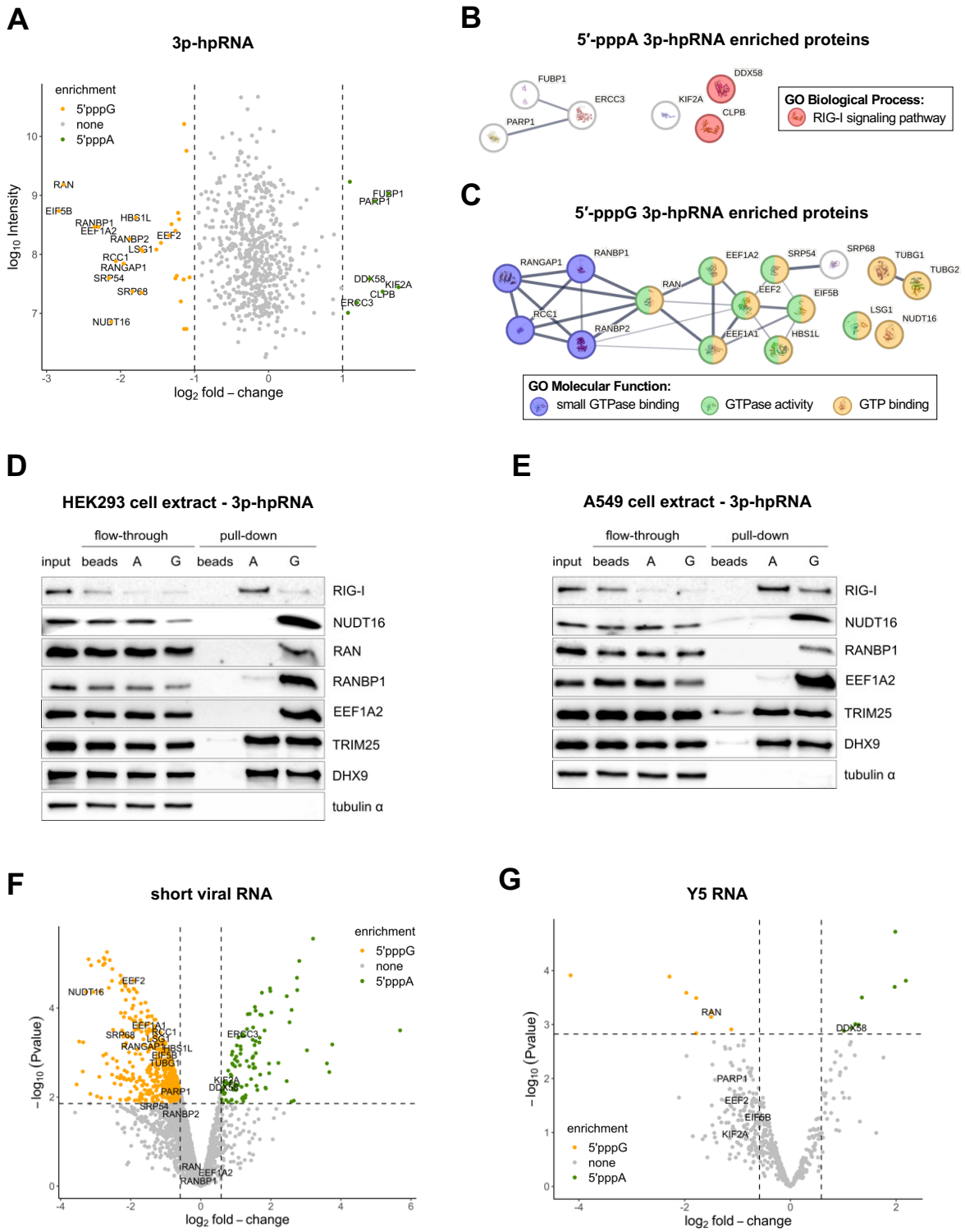

Fig. 6. Difference in binding affinities of proteins to 5′-pppA and 5′-pppG RNAs. (**A**) RNA pull-down analysis using 5′-pppA or 5′-pppG 3p-hpRNA and SILAC-labelled HEK293 cell extract followed by Mass Spectrometry analysis. 5′-pppA and 5′-pppG 3p-hpRNA enriched proteins with at least 2-fold change are depicted as green and orange, respectively. (**B,**

C) STRING Functional Enrichment Analysis of 5′-pppA (**B**) and 5′-pppG (**C**) 3p-hpRNA enriched proteins. (**D**, **E**) RNA pull-down followed by Western blot analysis using 5′-pppA and 5′-pppG 3p-hpRNAs and HEK293 and A549 cell extracts. TRIM25 and DHX9 were used as RNA pull-down quality controls, and α-tubulin was used as a loading control. (**F**, **G**) RNA pull-down coupled with label-free quantitative mass spectrometry of 5′-pppA *vs.* 5′-pppG short viral RNA and Y5 RNA. 5′-pppA and 5′-pppG enriched proteins with at least 1.5-fold change and P_{adj} <0.05 are depicted as green and orange, respectively.

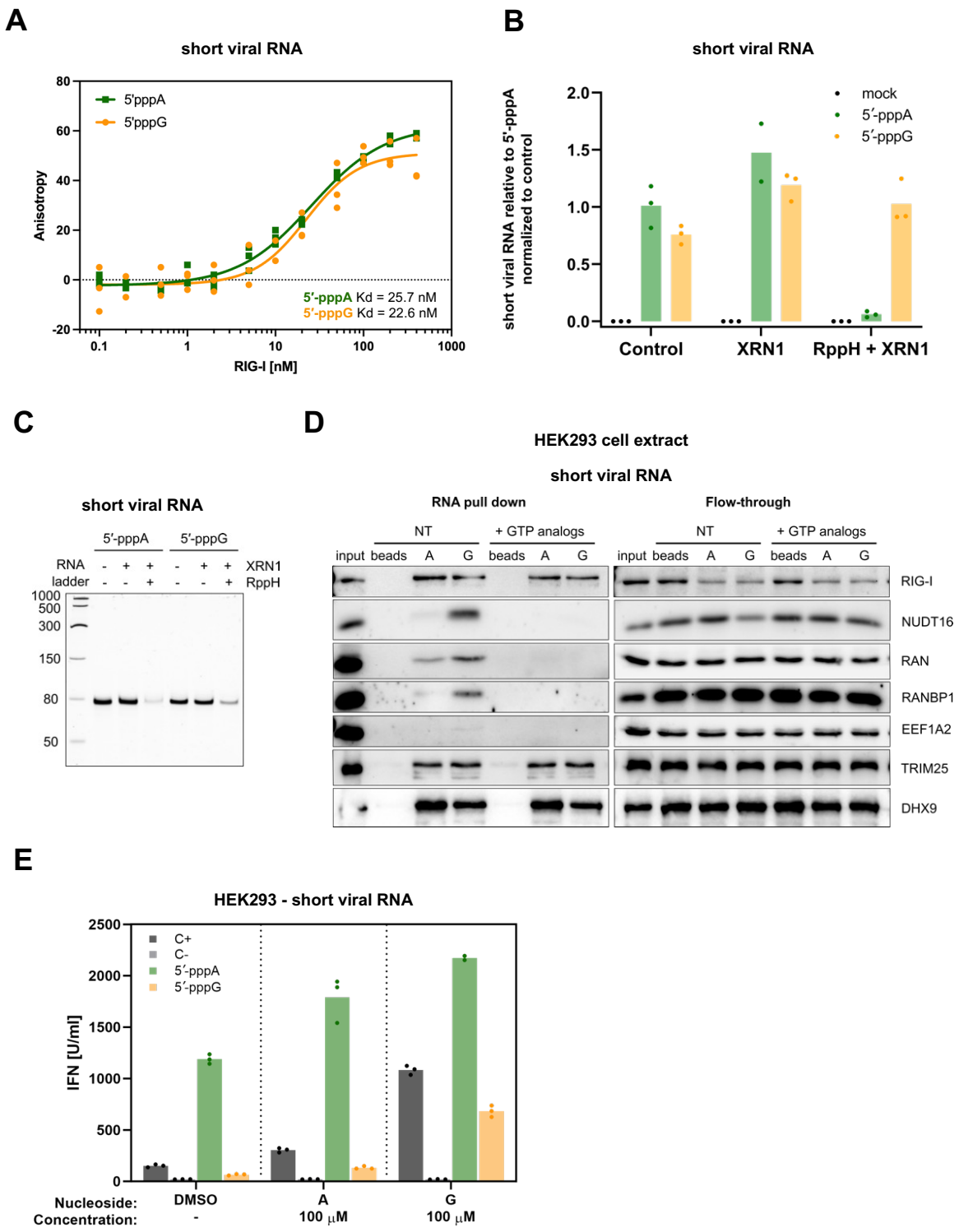

Fig. 7. Proteins with GTP binding and GTPase activity bind to and shield 5′-pppG RNAs from RIG-I recognition. (**A**) Fluorescence anisotropy analysis with internally fluorescein-labelled 5′-pppA or 5′-pppG short viral RNAs and increasing quantities of RIG-I protein (in the range of 0.1 to 1000 nM) was performed. The dissociation constant (K_d) was calculated as

the concentration of RIG-I protein, at which anisotropy reaches half of the equilibrium state value. Three biological replicates are shown. (**B, C**) *In vivo* (**B**) and *in vitro* (**C**) analysis of phosphorylation state of 5′-pppA *vs.* 5′-pppG short viral RNAs. (**B**) HEK293 cells were transfected with 100 ng/ml of tested RNAs, then total RNA was purified followed by exonuclease XRN-1 or pyrophosphohydrolase RppH and XRN-1 combined treatment. RT-qPCR was used to assess the level of short viral RNA (for each treatment variant n=3). (**C**) IVT derived 5′-pppA or 5′-pppG short viral RNAs were treated with XRN-1 or RppH and XRN-1 and then PAGE/urea was performed to visualize the level of RNAs which were resistant to XRN-1 exoribonucleolytic activity. (**D**) 5′-pppA *vs.* 5′-pppG short viral RNA pull-down analysis combined with nonhydrolyzable GTP analogs supplementation. GTP analogs were added to the beads-RNA-HEK293 cell extracts mixtures at 0.5 mM concentration. Representative Western blot analysis is shown. (**E**) Induction of nucleotide salvage pathway leads to higher 5′-pppG-stimulated IFN activity. HEK293 cells were supplemented with 100 μM guanosine, 100 μM adenosine or DMSO. After 48 h the cells were transfected with 100 ng/ml 5′-pppA or 5′-pppG short viral RNAs and incubated for another 24 h followed by IFN assay. Three biological replicates are shown.

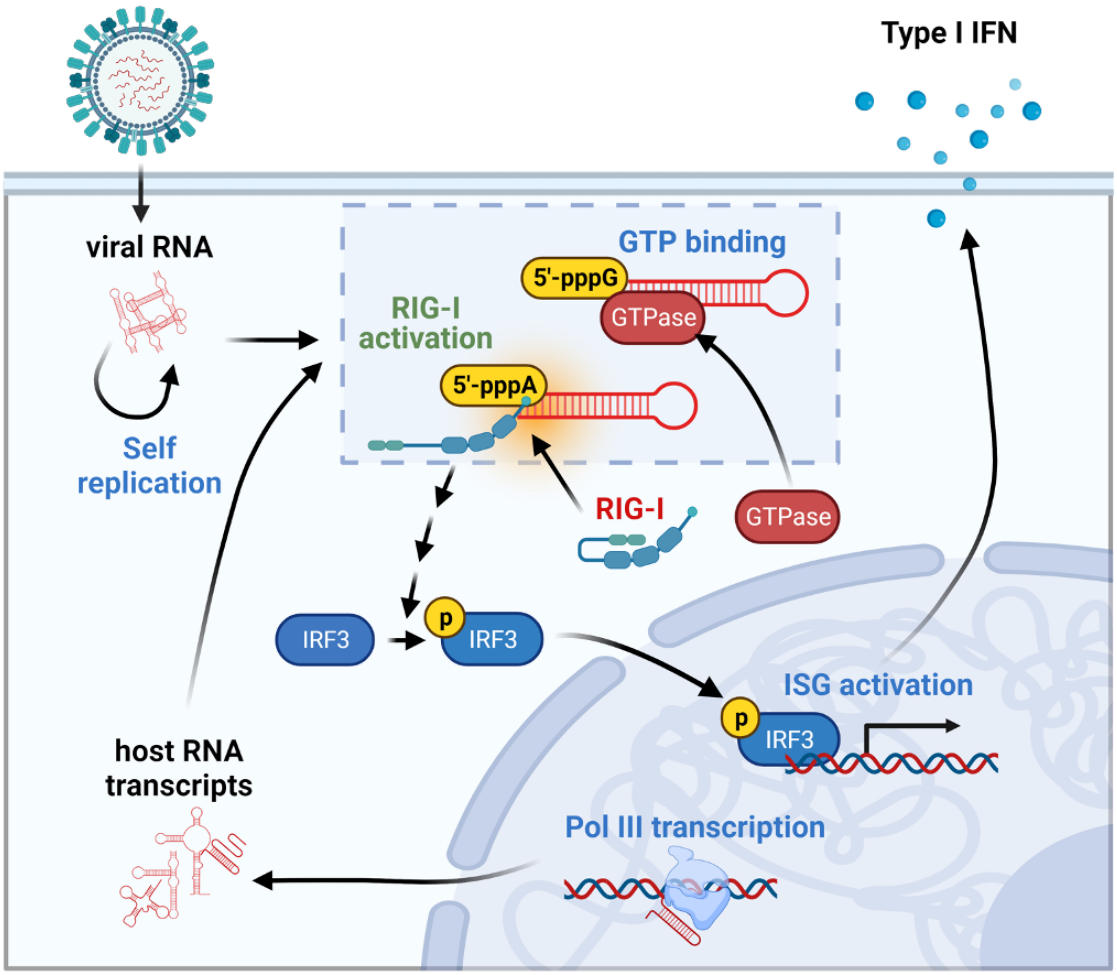

Fig. 8. A model for sequence-specific sensing of RNAs by RIG-I. Viral RNA upon entry to the host cells undergoes self-amplification. RIG-I may sense Pol III transcripts and viral RNAs starting with 5′-pppA. This recognition triggers a cascade of events, including IRF3 phosphorylation, ISG activation, and the subsequent production of type I IFN. RNAs containing a terminal nucleotide of 5′-pppG are identified by GTPases and GTP-binding proteins, which subsequently obstruct their recognition by the RIG-I/IFN pathway.

References

1. Rehwinkel, J., and Gack, M.U. (2020). RIG-I-like receptors: their regulation and roles in RNA sensing. Nat Rev Immunol *20*, 537-551. 10.1038/s41577-020-0288-3.
2. Hornung, V., Ellegast, J., Kim, S., Brzozka, K., Jung, A., Kato, H., Poeck, H., Akira, S., Conzelmann, K.K., Schlee, M., et al. (2006). 5'-Triphosphate RNA is the ligand for RIG-I. Science *314*, 994-997. 10.1126/science.1132505.
3. Wang, W., Gotte, B., Guo, R., and Pyle, A.M. (2023). The E3 ligase Riplet promotes RIG-I signaling independent of RIG-I oligomerization. Nat Commun *14*, 7308. 10.1038/s41467-023-42982-0.
4. Cadena, C., Ahmad, S., Xavier, A., Willemsen, J., Park, S., Park, J.W., Oh, S.W., Fujita, T., Hou, F., Binder, M., and Hur, S. (2019). Ubiquitin-Dependent and -Independent Roles of E3 Ligase RIPLET in Innate Immunity. Cell *177*, 1187-1200 e1116. 10.1016/j.cell.2019.03.017.
5. Thoresen, D., Wang, W., Galls, D., Guo, R., Xu, L., and Pyle, A.M. (2021). The molecular mechanism of RIG-I activation and signaling. Immunol Rev *304*, 154-168. 10.1111/imr.13022.
6. Shaw, A.E., Hughes, J., Gu, Q., Behdenna, A., Singer, J.B., Dennis, T., Orton, R.J., Varela, M., Gifford, R.J., Wilson, S.J., and Palmarini, M. (2017). Fundamental properties of the mammalian innate immune system revealed by multispecies comparison of type I interferon responses. PLoS Biol *15*, e2004086. 10.1371/journal.pbio.2004086.
7. Barrat, F.J., Elkon, K.B., and Fitzgerald, K.A. (2016). Importance of Nucleic Acid Recognition in Inflammation and Autoimmunity. Annu Rev Med *67*, 323-336. 10.1146/annurev-med-052814-023338.
8. Goubau, D., Schlee, M., Deddouche, S., Pruijssers, A.J., Zillinger, T., Goldeck, M., Schuberth, C., Van der Veen, A.G., Fujimura, T., Rehwinkel, J., et al. (2014). Antiviral immunity via RIG-I-mediated recognition of RNA bearing 5'-diphosphates. Nature *514*, 372-375. 10.1038/nature13590.
9. Schlee, M., Roth, A., Hornung, V., Hagmann, C.A., Wimmenauer, V., Barchet, W., Coch, C., Janke, M., Mihailovic, A., Wardle, G., et al. (2009). Recognition of 5' triphosphate by RIG-I helicase requires short blunt double-stranded RNA as contained in panhandle of negative-strand virus. Immunity *31*, 25-34. 10.1016/j.immuni.2009.05.008.
10. Myong, S., Cui, S., Cornish, P.V., Kirchhofer, A., Gack, M.U., Jung, J.U., Hopfner, K.P., and Ha, T. (2009). Cytosolic viral sensor RIG-I is a 5'-triphosphate-dependent translocase on double-stranded RNA. Science *323*, 1070-1074. 10.1126/science.1168352.
11. Ren, X., Linehan, M.M., Iwasaki, A., and Pyle, A.M. (2019). RIG-I Selectively Discriminates against 5'-Monophosphate RNA. Cell Rep *26*, 2019-2027 e2014. 10.1016/j.celrep.2019.01.107.
12. Schuberth-Wagner, C., Ludwig, J., Bruder, A.K., Herzner, A.M., Zillinger, T., Goldeck, M., Schmidt, T., Schmid-Burgk, J.L., Kerber, R., Wolter, S., et al. (2015). A Conserved Histidine in the RNA Sensor RIG-I Controls Immune Tolerance to N1-2'O-Methylated Self RNA. Immunity *43*, 41-51. 10.1016/j.immuni.2015.06.015.
13. Tockary, T.A., Abbasi, S., Matsui-Masai, M., Hayashi, A., Yoshinaga, N., Boonstra, E., Wang, Z., Fukushima, S., Kataoka, K., and Uchida, S. (2023). Comb-structured mRNA vaccine tethered with short double-stranded RNA adjuvants maximizes cellular immunity for cancer treatment. Proc Natl Acad Sci U S A *120*, e2214320120. 10.1073/pnas.2214320120.

14. Linehan, M.M., Dickey, T.H., Molinari, E.S., Fitzgerald, M.E., Potapova, O., Iwasaki, A., and Pyle, A.M. (2018). A minimal RNA ligand for potent RIG-I activation in living mice. Sci Adv *4*, e1701854. 10.1126/sciadv.1701854.
15. Te Velthuis, A.J.W., Long, J.C., Bauer, D.L.V., Fan, R.L.Y., Yen, H.L., Sharps, J., Siegers, J.Y., Killip, M.J., French, H., Oliva-Martin, M.J., et al. (2018). Mini viral RNAs act as innate immune agonists during influenza virus infection. Nat Microbiol *3*, 1234-1242. 10.1038/s41564-018-0240-5.
16. Schlee, M. (2013). Master sensors of pathogenic RNA - RIG-I like receptors. Immunobiology *218*, 1322-1335. 10.1016/j.imbio.2013.06.007.
17. Ma, H., Wu, Y., Dang, Y., Choi, J.G., Zhang, J., and Wu, H. (2014). Pol III Promoters to Express Small RNAs: Delineation of Transcription Initiation. Mol Ther Nucleic Acids *3*, e161. 10.1038/mtna.2014.12.
18. Gao, Z., Harwig, A., Berkhout, B., and Herrera-Carrillo, E. (2017). Mutation of nucleotides around the +1 position of type 3 polymerase III promoters: The effect on transcriptional activity and start site usage. Transcription *8*, 275-287. 10.1080/21541264.2017.1322170.
19. Marq, J.B., Kolakofsky, D., and Garcin, D. (2010). Unpaired 5' ppp-nucleotides, as found in arenavirus double-stranded RNA panhandles, are not recognized by RIG-I. J Biol Chem *285*, 18208-18216. 10.1074/jbc.M109.089425.
20. Sherwood, A.V., Rivera-Rangel, L.R., Ryberg, L.A., Larsen, H.S., Anker, K.M., Costa, R., Vagbo, C.B., Jakljevic, E., Pham, L.V., Fernandez-Antunez, C., et al. (2023). Hepatitis C virus RNA is 5'-capped with flavin adenine dinucleotide. Nature *619*, 811-818. 10.1038/s41586-023-06301-3.
21. Deflube, L.R., Cressey, T.N., Hume, A.J., Olejnik, J., Haddock, E., Feldmann, F., Ebihara, H., Fearns, R., and Muhlberger, E. (2019). Ebolavirus polymerase uses an unconventional genome replication mechanism. Proc Natl Acad Sci U S A *116*, 8535-8543. 10.1073/pnas.1815745116.
22. Turowski, T.W., and Tollervey, D. (2016). Transcription by RNA polymerase III: insights into mechanism and regulation. Biochem Soc Trans *44*, 1367-1375. 10.1042/BST20160062.
23. Schlee, M., and Hartmann, G. (2010). The chase for the RIG-I ligand--recent advances. Mol Ther *18*, 1254-1262. 10.1038/mt.2010.90.
24. Deng, T., Vreede, F.T., and Brownlee, G.G. (2006). Different de novo initiation strategies are used by influenza virus RNA polymerase on its cRNA and viral RNA promoters during viral RNA replication. J Virol *80*, 2337-2348. 10.1128/JVI.80.5.2337-2348.2006.
25. Cai, Z., Liang, T.J., and Luo, G. (2004). Effects of mutations of the initiation nucleotides on hepatitis C virus RNA replication in the cell. J Virol *78*, 3633-3643. 10.1128/jvi.78.7.3633-3643.2004.
26. Kowalski, M.P., and Krude, T. (2015). Functional roles of non-coding Y RNAs. Int J Biochem Cell Biol *66*, 20-29. 10.1016/j.biocel.2015.07.003.
27. Vabret, N., Najburg, V., Solovyov, A., Gopal, R., McClain, C., Sulc, P., Balan, S., Rahou, Y., Beauclair, G., Chazal, M., et al. (2022). Y RNAs are conserved endogenous RIG-I ligands across RNA virus infection and are targeted by HIV-1. iScience *25*, 104599. 10.1016/j.isci.2022.104599.
28. Gendron, M., Roberge, D., and Boire, G. (2001). Heterogeneity of human Ro ribonucleoproteins (RNPS): nuclear retention of Ro RNPS containing the human hY5 RNA in human and mouse cells. Clin Exp Immunol *125*, 162-168. 10.1046/j.1365-2249.2001.01566.x.

29. Marques, J.T., Devosse, T., Wang, D., Zamanian-Daryoush, M., Serbinowski, P., Hartmann, R., Fujita, T., Behlke, M.A., and Williams, B.R. (2006). A structural basis for discriminating between self and nonself double-stranded RNAs in mammalian cells. Nat Biotechnol *24*, 559-565. 10.1038/nbt1205.
30. Schmidt, A., Schwerd, T., Hamm, W., Hellmuth, J.C., Cui, S., Wenzel, M., Hoffmann, F.S., Michallet, M.C., Besch, R., Hopfner, K.P., et al. (2009). 5'-triphosphate RNA requires base-paired structures to activate antiviral signaling via RIG-I. Proc Natl Acad Sci U S A *106*, 12067-12072. 10.1073/pnas.0900971106.
31. Zuker, M. (2003). Mfold web server for nucleic acid folding and hybridization prediction. Nucleic Acids Res *31*, 3406-3415. 10.1093/nar/gkg595.
32. Boccitto, M., and Wolin, S.L. (2019). Ro60 and Y RNAs: structure, functions, and roles in autoimmunity. Crit Rev Biochem Mol Biol *54*, 133-152. 10.1080/10409238.2019.1608902.
33. Konarska, M.M., and Sharp, P.A. (1989). Replication of RNA by the DNA-dependent RNA polymerase of phage T7. Cell *57*, 423-431. 10.1016/0092-8674(89)90917-3.
34. Mu, X., Greenwald, E., Ahmad, S., and Hur, S. (2018). An origin of the immunogenicity of in vitro transcribed RNA. Nucleic Acids Res *46*, 5239-5249. 10.1093/nar/gky177.
35. Choudhury, N.R., and Michlewski, G. (2019). Quantitative identification of proteins that influence miRNA biogenesis by RNA pull-down-SILAC mass spectrometry (RP-SMS). Methods *152*, 12-17. 10.1016/j.ymeth.2018.06.006.
36. Choudhury, N.R., Trus, I., Heikel, G., Wolczyk, M., Szymanski, J., Bolembach, A., Dos Santos Pinto, R.M., Smith, N., Trubitsyna, M., Gaunt, E., et al. (2022). TRIM25 inhibits influenza A virus infection, destabilizes viral mRNA, but is redundant for activating the RIG-I pathway. Nucleic Acids Res *50*, 7097-7114. 10.1093/nar/gkac512.
37. Choudhury, N.R., Heikel, G., and Michlewski, G. (2020). TRIM25 and its emerging RNA-binding roles in antiviral defense. Wiley Interdiscip Rev RNA *11*, e1588. 10.1002/wrna.1588.
38. Fullam, A., and Schroder, M. (2013). DExD/H-box RNA helicases as mediators of anti-viral innate immunity and essential host factors for viral replication. Biochim Biophys Acta *1829*, 854-865. 10.1016/j.bbagrm.2013.03.012.
39. Foley, P.L., Hsieh, P.K., Luciano, D.J., and Belasco, J.G. (2015). Specificity and evolutionary conservation of the Escherichia coli RNA pyrophosphohydrolase RppH. J Biol Chem *290*, 9478-9486. 10.1074/jbc.M114.634659.
40. Chandel, N.S. (2021). Nucleotide Metabolism. Cold Spring Harb Perspect Biol *13*. 10.1101/cshperspect.a040592.
41. Pastor-Anglada, M., and Perez-Torras, S. (2018). Emerging Roles of Nucleoside Transporters. Front Pharmacol *9*, 606. 10.3389/fphar.2018.00606.
42. Hoffmann, H.H., Schneider, W.M., and Rice, C.M. (2015). Interferons and viruses: an evolutionary arms race of molecular interactions. Trends Immunol *36*, 124-138. 10.1016/j.it.2015.01.004.
43. Ficarelli, M., Antzin-Anduetza, I., Hugh-White, R., Firth, A.E., Sertkaya, H., Wilson, H., Neil, S.J.D., Schulz, R., and Swanson, C.M. (2020). CpG Dinucleotides Inhibit HIV-1 Replication through Zinc Finger Antiviral Protein (ZAP)-Dependent and -Independent Mechanisms. J Virol *94*. 10.1128/JVI.01337-19.
44. Streicher, F., and Jouvenet, N. (2019). Stimulation of Innate Immunity by Host and Viral RNAs. Trends Immunol *40*, 1134-1148. 10.1016/j.it.2019.10.009.
45. Devarkar, S.C., Wang, C., Miller, M.T., Ramanathan, A., Jiang, F., Khan, A.G., Patel, S.S., and Marcotrigiano, J. (2016). Structural basis for m7G recognition and 2'-O-

methyl discrimination in capped RNAs by the innate immune receptor RIG-I. Proc Natl Acad Sci U S A *113*, 596-601. 10.1073/pnas.1515152113.
46. Choi, J.H., Burke, J.M., Szymanik, K.H., Nepal, U., Battenhouse, A., Lau, J.T., Stark, A., Lam, V., and Sullivan, C.S. (2020). DUSP11-mediated control of 5'-triphosphate RNA regulates RIG-I sensitivity. Genes Dev *34*, 1697-1712. 10.1101/gad.340604.120.
47. Ren, X., Linehan, M.M., Iwasaki, A., and Pyle, A.M. (2019). RIG-I Recognition of RNA Targets: The Influence of Terminal Base Pair Sequence and Overhangs on Affinity and Signaling. Cell Rep *29*, 3807-3815 e3803. 10.1016/j.celrep.2019.11.052.
48. Gunter, H.M., Idrisoglu, S., Singh, S., Han, D.J., Ariens, E., Peters, J.R., Wong, T., Cheetham, S.W., Xu, J., Rai, S.K., et al. (2023). mRNA vaccine quality analysis using RNA sequencing. Nat Commun *14*, 5663. 10.1038/s41467-023-41354-y.
49. Baiersdorfer, M., Boros, G., Muramatsu, H., Mahiny, A., Vlatkovic, I., Sahin, U., and Kariko, K. (2019). A Facile Method for the Removal of dsRNA Contaminant from In Vitro-Transcribed mRNA. Mol Ther Nucleic Acids *15*, 26-35. 10.1016/j.omtn.2019.02.018.
50. Triana-Alonso, F.J., Dabrowski, M., Wadzack, J., and Nierhaus, K.H. (1995). Self-coded 3'-extension of run-off transcripts produces aberrant products during in vitro transcription with T7 RNA polymerase. J Biol Chem *270*, 6298-6307. 10.1074/jbc.270.11.6298.
51. Rosa, M.D., Gottlieb, E., Lerner, M.R., and Steitz, J.A. (1981). Striking similarities are exhibited by two small Epstein-Barr virus-encoded ribonucleic acids and the adenovirus-associated ribonucleic acids VAI and VAII. Mol Cell Biol *1*, 785-796. 10.1128/mcb.1.9.785-796.1981.
52. Quaglia, M., Merlotti, G., De Andrea, M., Borgogna, C., and Cantaluppi, V. (2021). Viral Infections and Systemic Lupus Erythematosus: New Players in an Old Story. Viruses *13*. 10.3390/v13020277.
53. Gakis, G., Angelopoulos, I., Panagoulias, I., and Mouzaki, A. (2023). Current knowledge on multiple sclerosis pathophysiology, disability progression assessment and treatment options, and the role of autologous hematopoietic stem cell transplantation. Autoimmun Rev, 103480. 10.1016/j.autrev.2023.103480.
54. Takei, M., Kitamura, N., Nagasawa, Y., Tsuzuki, H., Iwata, M., Nagatsuka, Y., Nakamura, H., Imai, K., and Fujiwara, S. (2022). Are Viral Infections Key Inducers of Autoimmune Diseases? Focus on Epstein-Barr Virus. Viruses *14*. 10.3390/v14091900.
55. Weis, S., and Te Velthuis, A.J.W. (2021). Influenza Virus RNA Synthesis and the Innate Immune Response. Viruses *13*. 10.3390/v13050780.
56. Vasilyev, N., and Serganov, A. (2016). Preparation of Short 5'-Triphosphorylated Oligoribonucleotides for Crystallographic and Biochemical Studies. Methods Mol Biol *1320*, 11-20. 10.1007/978-1-4939-2763-0_2.
57. Bravo, J.I., Kim, M., and Benayoun, B.A. (2021). Protocol for isolation of adult mouse ear pinnae-derived primary fibroblasts. STAR Protoc *2*, 100406. 10.1016/j.xpro.2021.100406.
58. Slusarczyk, P., Mandal, P.K., Zurawska, G., Niklewicz, M., Chouhan, K., Mahadeva, R., Jonczy, A., Macias, M., Szybinska, A., Cybulska-Lubak, M., et al. (2023). Impaired iron recycling from erythrocytes is an early hallmark of aging. Elife *12*. 10.7554/eLife.79196.
59. Rebendenne, A., Valadao, A.L.C., Tauziet, M., Maarifi, G., Bonaventure, B., McKellar, J., Planes, R., Nisole, S., Arnaud-Arnould, M., Moncorge, O., and Goujon, C. (2021). SARS-CoV-2 triggers an MDA-5-dependent interferon response which is unable to control replication in lung epithelial cells. J Virol *95*. 10.1128/JVI.02415-20.

60. Mejia-Calvo, I., Munoz-Garcia, L., Jimenez-Uribe, A., Camacho-Sandoval, R., Gonzalez-Gonzalez, E., Mellado-Sanchez, G., Tenorio-Calvo, A.V., Lopez-Morales, C.A., Velasco-Velazquez, M.A., Pavon, L., et al. (2019). Validation of a cell-based colorimetric reporter gene assay for the evaluation of Type I Interferons. Biotechnol Rep (Amst) *22*, e00331. 10.1016/j.btre.2019.e00331.
61. Motulsky, H.J., and Brown, R.E. (2006). Detecting outliers when fitting data with nonlinear regression - a new method based on robust nonlinear regression and the false discovery rate. BMC Bioinformatics *7*, 123. 10.1186/1471-2105-7-123.
62. Busan, S., and Weeks, K.M. (2018). Accurate detection of chemical modifications in RNA by mutational profiling (MaP) with ShapeMapper 2. RNA *24*, 143-148. 10.1261/rna.061945.117.
63. Ritchie, M.E., Phipson, B., Wu, D., Hu, Y., Law, C.W., Shi, W., and Smyth, G.K. (2015). limma powers differential expression analyses for RNA-sequencing and microarray studies. Nucleic Acids Res *43*, e47. 10.1093/nar/gkv007.
64. Traut, T.W. (1994). Physiological concentrations of purines and pyrimidines. Mol Cell Biochem *140*, 1-22. 10.1007/BF00928361.
65. Shevchenko, A., Wilm, M., Vorm, O., and Mann, M. (1996). Mass spectrometric sequencing of proteins silver-stained polyacrylamide gels. Anal Chem *68*, 850-858. 10.1021/ac950914h.
66. Rappsilber, J., Mann, M., and Ishihama, Y. (2007). Protocol for micro-purification, enrichment, pre-fractionation and storage of peptides for proteomics using StageTips. Nat Protoc *2*, 1896-1906. 10.1038/nprot.2007.261.
67. Olsen, J.V., Macek, B., Lange, O., Makarov, A., Horning, S., and Mann, M. (2007). Higher-energy C-trap dissociation for peptide modification analysis. Nat Methods *4*, 709-712. 10.1038/nmeth1060.
68. Cox, J., and Mann, M. (2008). MaxQuant enables high peptide identification rates, individualized p.p.b.-range mass accuracies and proteome-wide protein quantification. Nat Biotechnol *26*, 1367-1372. 10.1038/nbt.1511.
69. Cox, J., Neuhauser, N., Michalski, A., Scheltema, R.A., Olsen, J.V., and Mann, M. (2011). Andromeda: a peptide search engine integrated into the MaxQuant environment. J Proteome Res *10*, 1794-1805. 10.1021/pr101065j.
70. Demichev, V., Messner, C.B., Vernardis, S.I., Lilley, K.S., and Ralser, M. (2020). DIA-NN: neural networks and interference correction enable deep proteome coverage in high throughput. Nat Methods *17*, 41-44. 10.1038/s41592-019-0638-x.
71. Quast, J.P., Schuster, D., and Picotti, P. (2022). protti: an R package for comprehensive data analysis of peptide- and protein-centric bottom-up proteomics data. Bioinform Adv *2*, vbab041. 10.1093/bioadv/vbab041.
72. Kuzniewska, B., Rejmak, K., Nowacka, A., Ziolkowska, M., Milek, J., Magnowska, M., Gruchota, J., Gewartowska, O., Borsuk, E., Salamian, A., et al. (2022). Disrupting interaction between miR-132 and Mmp9 3'UTR improves synaptic plasticity and memory in mice. Front Mol Neurosci *15*, 924534. 10.3389/fnmol.2022.924534.
73. Behringer, R., Gertsenstein, M., Nagy, K.V., and Nagy, A. (2019). Preparation of Polymerase Chain Reaction Template DNA from Mouse Tail Tissue. Cold Spring Harb Protoc *2019*. 10.1101/pdb.prot092700.
74. Wang, X., Liu, S., Sun, Y., Yu, X., Lee, S.M., Cheng, Q., Wei, T., Gong, J., Robinson, J., Zhang, D., et al. (2023). Preparation of selective organ-targeting (SORT) lipid nanoparticles (LNPs) using multiple technical methods for tissue-specific mRNA delivery. Nat Protoc *18*, 265-291. 10.1038/s41596-022-00755-x.
75. Perez-Riverol, Y., Bai, J., Bandla, C., Garcia-Seisdedos, D., Hewapathirana, S., Kamatchinathan, S., Kundu, D.J., Prakash, A., Frericks-Zipper, A., Eisenacher, M., et

al. (2022). The PRIDE database resources in 2022: a hub for mass spectrometry-based proteomics evidences. Nucleic Acids Res *50*, D543-D552. 10.1093/nar/gkab1038.

76. Crooks, G.E., Hon, G., Chandonia, J.M., and Brenner, S.E. (2004). WebLogo: a sequence logo generator. Genome Res *14*, 1188-1190. 10.1101/gr.849004.

77. Reuter, J.S., and Mathews, D.H. (2010). RNAstructure: software for RNA secondary structure prediction and analysis. BMC Bioinformatics *11*, 129. 10.1186/1471-2105-11-129.